The Magellanic Stream and Debris Clouds

B.-Q. For[1,2], L. Staveley-Smith[1], D. Matthews[3], N. M. McClure-Griffiths[4]

[1]*International Centre for Radio Astronomy Research, University of Western Australia, 35 Stirling Hwy, Crawley, WA, 6009, Australia; biqing.for@icrar.org*

[3]*Centre for Materials and Surface Science, La Trobe University, Melbourne, VIC, 3086, Australia*

[4]*CSIRO Astronomy and Space Science, Epping, NSW, 1710, Australia*

ABSTRACT

We present a study of the discrete clouds and filaments in the Magellanic Stream using a new high-resolution survey of neutral hydrogen (H I) conducted with H75 array of the Australia Telescope Compact Array, complemented by single-dish data from the Parkes Galactic All-Sky Survey (GASS). From the individual and combined datasets, we have compiled a catalog of 251 clouds and list their basic parameters, including a morphological description useful for identifying cloud interactions. We find an unexpectedly large number of head-tail clouds in the region. The implication for the formation mechanism and evolution is discussed. The filaments appear to originate entirely from the Small Magellanic Cloud and extend into the northern end of the Magellanic Bridge.

Subject headings: Galaxy: halo – intergalactic medium – ISM: H I– Magellanic Clouds

1. INTRODUCTION

The Magellanic Clouds (MCs) are the closest extragalactic neighbors to our Galaxy. Their gaseous component was discovered in atomic hydrogen as a coherent stream originating from the MCs, namely the Magellanic Stream (MS; Wannier & Wrixon 1972; Mathewson et al. 1974) and Leading Arm (LA; Putman et al. 1998). The MS is trailing the MCs and has been subdivided into six main concentrations (MS I–VI) (Mathewson et al. 1974). Although this

---

[2]SIEF John Stocker Fellow

subdivision is an oversimplification, it is widely used to describe different regions along the stream in the literature.

Recent detailed studies around the outskirt of the MS have made new discoveries. Several new filaments that are parallel with the MS (Westmeier & Koribalski 2008) and extended near the northern tip of the MS (Nidever et al. 2010) have been found. These suggest that the MS and LA now spans a total of $\sim 200°$ in length across the sky and is $\sim 30°$ wide at its widest point. The LA, a counterpart of the MS, is leading the H I gas stream and is morphologically very different from the MS. It is dominated by three distinctive high-velocity cloud (HVC) complexes (LA I–III; Putman et al. 1998; Brüns et al. 2005), and LA IV which is formed by a population of HVCs as defined by For et al. (2013; hereafter FSM13), or as a single HVC complex defined by Venzmer et al. (2012).

The formation and origin of the MS and LA are still under debate. There are two well-studied physical mechanisms that may be the cause for the formation of the MS and LA: ram-pressure stripping of gas from the MCs due to interaction with the Galactic halo (e.g., Moore & Davis 1994; Mastropietro et al. 2005), and tidal interaction between the Milky Way and the MCs (e.g., Gardiner & Noguchi 1996; Connors et al. 2006). Both scenarios were modeled and required orbits to reproduce the global observed H I column density and velocity distribution of the MS and LA. High-precision Hubble Space Telescope (HST) proper motion measurements of the MCs (Kallivayalil et al. 2006a,b, 2013) favor either an unbound orbit for the MCs with a first passage scenario (Besla et al. 2007) or an eccentric long period orbit (Shattow & Loeb 2009). The proposed new scenarios based on the HST proper motion measurements draw controversy as tidal and ram-pressure stripping require the MCs to be relatively close to the Milky Way for a long interaction time (multiple orbits). However, recent simulations have shown that tidal force of the LMC acting on the SMC alone can create the MS and LA before the MCs were accreted by the Milky Way in the first passage scenario (Besla et al. 2012; Diaz & Bekki 2012). Simulations with a bound orbit and extra drag have also successfully reproduced the observed bifurcation of the MS and remain consistent with the second epoch proper motion data (Diaz & Bekki 2011). A blowout hypothesis has been proposed by Nidever et al. (2008). They suggest that the supergiant shells in the southeast HI overdensity region of the LMC are blown out to larger radii where ram-pressure and/or tidal forces can more easily strip the gas into the MS and LA. Connections between gas in the LMC and the Bridge, Stream and Leading Arm have previously been pointed by other authors (McGee & Newton 1986; Putman et al. 1998, 2003; Staveley-Smith et al. 2003), though not as the main source of gas feeding the stream.

An observational approach to trace the origin of the MS and LA uses metallicity measurements as an indicator. Early studies of metallicity measurements from the HST spectra of

background sources toward the MS and LA II constrain their origin to the MCs ($Z = 0.2 - 0.4$ solar; Lu et al. 1994, 1998; Gibson et al. 2000). Subsequent studies with the HST and/or FUSE spectra suggest that the MS and LA originate from the SMC (Sembach et al. 2001; Fox et al. 2010). Recent metallicity measurements based on the VLT/UVES and HST/COS spectra of four background active galactic nuclei strongly support a scenario of which most of the stream gas were stripped from the SMC (Fox et al. 2013). However, a subsequent study of the same series reports a much higher metallicity (S/H =0.5 solar) in the inner Stream toward background quasar, Fairall 9 (Richter et al. 2013). The overall chemical abundances of MS toward Fairall 9 are significantly different as compared to other sight-lines suggest a complex enrichment history of the stream. They favor the explanation of local α-enrichment by massive stars followed by separation from the MCs before nitrogen enrichment occurs. They also state that the finding supports the dual-origin as identified by Nidever et al. (2008) but is not a requirement. Nevertheless, there is still a short-coming in the ability of theoretical models to reproduce the general observed LA features and complex filamentary structure of the MS. Physical properties of HVCs, such as the multiphase structures formed via hydrodynamical interactions with the hot halo, are seldom able to be considered in simulations.

Large-scale H I surveys have provided huge amounts of information for studying the gaseous structures surrounding our Milky Way. The most notable surveys are the H I Parkes All-Sky Survey (HIPASS; Barnes et al. 2001), the Leiden-Argentine-Bonn all-sky H I survey (LAB; Kalberla et al. 2005) and the Galactic All-Sky Survey (GASS; McClure-Griffiths et al. 2009) in the Southern hemisphere. HIPASS is an extragalactic survey with a coarse velocity resolution ($\Delta v \sim 18$ km s^{-1}) but is very sensitive and covers a large range in velocity. The data were employed to create an HVC catalog (Putman et al. 2002, hereafter P02) and to recover the extended structure of the Magellanic System (Putman et al. 2003). GASS is a Galactic survey with a much better spectral resolution ($\Delta v = 1$ km s^{-1}) and far more suitable to study the gaseous feature of the Magellanic System. LAB also has good spectral resolution ($\Delta v \sim 1.3$ km s^{-1}) but less angular resolution than GASS. The LAB data were employed by Nidever et al. (2008) for their study on the Magellanic System. Other smaller scale studies for the Magellanic System or subregions include, for example, the narrow-band Parkes H I survey (Brüns et al. 2005), H I Galactic studies with Arecibo L-band Feed Array (GALFA-HI; Stanimirović et al. 2008) and a Green Bank Telescope survey (Nidever et al. 2010).

In this paper we study the overall morphology of the MS using interferometric and single dish data, the general distribution, the physical properties and morphological properties of its HVCs. The aims are: (1) to understand the formation and origin of the MS, (2) to investigate the effect of interaction with the Galactic halo, and (3) to provide constraints

for simulations based on the observed properties. In §2 and §3, we describe the observations and the procedures for source finding. We present the catalog and cloud properties in §4 and §5. Cloud morphology, kinematic distribution and interpretation of the distributions are presented in §6. We discuss the implications of the HVCs on the formation of the MS by comparing the observed properties with theoretical models in §7. Summary and conclusions are given in §8.

2.   OBSERVATIONS AND DATA

A detailed description of the observing strategy and data reduction for the ATCA high-resolution Magellanic Stream survey is given in Matthews et al. (2014). A description of GASS is given by McClure-Griffiths et al. (2009) and Kalberla et al. (2010). A brief summary of the observations and characteristics of the data is given below.

The ATCA high-resolution Magellanic Stream survey covers a 500 deg^2 field of the MS using the H75 configuration of the ATCA. MS I to MS IV, part of Small Magellanic Cloud (SMC) and the Interface Region (IFR) are covered in this survey. The observations were carried out over a period from 2005 to 2006, which resulted in $\sim$180 hours of total observing time. The entire area was divided into 33 regions with 154 pointing centers per region, resulting in 5082 pointing centers. Each pointing center was separated by 20$'$, arranged in a hexagonal grid, observed for 20 s and revisited 6 times during an average of 10 hour observing. The resulting ATCA data have an angular resolution of 413$'' \times$ 330$''$, a brightness sensitivity of 210 mK and a velocity resolution of 1.65 km s^{-1} after Hanning smoothing. The survey covers Local Standard of Rest velocity (V_{LSR}) between -315 and $+393$ km s^{-1}.

GASS is an H I survey of the entire sky south of declination $+1°$ using the 20 cm multibeam receiver on the Parkes radio telescope. This survey covers V_{LSR} between -400 and $+500$ km s^{-1}. The second data release[1] employed in this study has been corrected for stray radiation and radio frequency interference, has a channel width of 0.82 km s^{-1}, a spectral resolution of 1 km s^{-1}, a brightness temperature (T_{B}) rms sensitivity of 57 mK and an angular resolution of 16$'$.

The reduced ATCA images are grouped into 11 data cubes (see Matthews et al. 2014 for the boundary of each data cube). To obtain the large-scale structure information missing from the interferometric data, Matthews et al. (2014) combined the ATCA data with the GASS data, hereafter H75GASS. The GASS data were matched to the angular dimensions of

---

[1]http://www.astro.uni-bonn.de/hisurvey/gass

each ATCA data cube prior merging. The data were merged in the image domain as detailed by Matthews et al. (2014). The merged data have an average T_B sensitivity of 250 mK, and are in equatorial coordinates.

To precisely and conveniently describe the position of various gaseous features along the MS, a Magellanic coordinate system has been used by many. For example, Wakker (2001) defined the north pole of the Magellanic coordinate system as Galactic longitude (l) 180° and latitude (b) 0°. Its equator passes through the Galactic equator at $l = 90°$ and $b = 270°$ and passes through the south Galactic pole. However, this definition does not place the equator exactly along the MS. A new coordinate system, Magellanic Stream coordinate, has since been introduced by Nidever et al. (2008) to better represent the projection of the MS along the equator. This new coordinate system defines $L_{MS} = 0°$ at the center of the Large Magellanic Cloud (LMC), i.e., $(l, b) = 280.47°, -32.75°$ (van der Marel et al. 2002), and the pole at $(l, b) = 188.5°, -7.5°$. The L_{MS} decreases in value toward the tip of the MS and increases in value toward the LA. We adopt this coordinate system for the rest of the paper.

3. SOURCE FINDING

3.1. Preparation

We converted the H75GASS data cubes into Galactic coordinates, with each covering a different range of velocities. To minimize the size of the data cubes, we created 12 subcubes covering the velocity range that contains obvious features of the MS. Any feature in the range -30 km s^{-1} $< V_{LSR} < +18$ km s^{-1} is indistinguishable from the strong Galactic H I emission and hence was excluded. Mild contamination from the Galactic H I emission occurs at $-40 \lesssim V_{LSR} \lesssim -30$ km s^{-1} and $+18 \lesssim V_{LSR} \lesssim +30$ km s^{-1}, which predominantly affects region $-55°$ to $-40°$ in L_{ms}. A mosaicked cube containing features of the MS at positive and negative LSR velocity was also created. A summary of velocity ranges for the original cubes and created subcubes is given in Table 1 (see Matthews et al. 2014 for the boundary of each data cube).

For the GASS data alone, we also extracted data cubes that covered a similar region and velocity range, giving a total of four data cubes (negative velocity and positive velocity for both H75GASS and GASS) for source finding. Integrated H I column density maps of the mosaicked H75GASS and GASS data are shown in Zenithal Equal Area (ZEA) projection in Figures 1 and 2.

3.2. Analysis

We performed the source finding using $Duchamp^2$ version 1.2.2, a 3-dimensional source finder developed by Whiting (2012). It is designed to search data cubes, merge detections and measure basic parameters of the detected sources. It also implements optional noise reduction routines, such as the wavelet reconstruction and spatial or spectral smoothing, to enhance the detectability of fainter sources.

Each of the input cubes was reconstructed with *à trous* wavelets to remove random noise prior to the search. A fixed threshold was specified for each run, and various thresholds were tested for each input cube to find the best source finding parameters. Sources were detected only if they extended across a minimum of 10 spatial pixels and ~ 5 km s^{-1} in velocity space (i.e., 5 and 3 velocity channels for GASS and H75GASS, respectively). Subsequently, the detected sources were compared to earlier detections and either merged with neighboring sources or added to the list as a single source.

Despite the application of noise reduction technique, diffuse emission was better detected with the GASS data alone. Thus, we decided to use the H75GASS and GASS data independently to detect compact and diffuse sources, respectively. A fixed threshold of $\sim 2\sigma$ above the background noise (57 mK) was employed for GASS positive and negative V_{LSR} cubes. We used fixed thresholds of $\sim 3\sigma$ above the background noise (250 mK) for the H75GASS negative and positive V_{LSR} cubes.

4. CATALOG

A compilation of sources with basic parameters is presented in Table 2. The catalog includes the following entries: the source identification number in Column 1; the designation with a prefix of HVC for high-velocity clouds and GLX for galaxies followed by the l, b and central V_{LSR} fitted with single Gaussian component in column 2; MS longitude (L_{MS}) and MS latitude (B_{MS}) in columns 3–4; central V_{LSR} in column 5; the central velocity in the Galactic Standard of Rest reference frame (V_{GSR}), defined by $V_{GSR} = 220 \cos b \sin l + V_{LSR}$; the velocity in the Local Group Standard of Rest reference frame (V_{LGSR}), defined by $V_{LGSR} = V_{GSR} - 62 \cos l \cos b + 40 \sin l \cos b - 35 \sin b$ (Braun & Burton 1999) in columns 6–7; velocity FWHM, measured at 50% of peak flux in column 8; integrated flux, peak T_{B} and peak H I column density (N_{HI}) in columns 9–11; semi-major axis, semi-minor axis and position angle in columns 12–14; warning flag, morphological classification, data origin and comment in

---

[2]Available at http://www.atnf.csiro.au/computing/software/duchamp/

columns 15–18.

We detected a total of 574 sources in our initial search. In the case of the same source being detected in both GASS and H75GASS cubes, we examined the spectrum and the adopted the parameters of the source with higher spectral signal-to-noise ratio. We also examined individual spectra and the data cube in order to eliminate false detections. Such detections are caused by background artifacts and noise peaks, which generally have a narrow line width. The positions of all final sources were examined using the NASA/IPAC Extragalactic Database to identify galaxies. 75 sources overlap with the Galactic emission channels and/or lie at the spatial edge of the image. These sources are included in the catalog but their physical parameters are omitted. The final catalog includes a total of 251 HVCs and 2 galaxies (NGC 300 and WLM). NGC 55 and NGC 7733 are positioned near the MS in the sky but are not detected because they do not fall into the field-of-view of ATCA survey. NGC 55 is shown in the extracted GASS data cube but lies on an artifact.

The *Duchamp* software derived most of the parameters listed above except angular sizes and peak H I column density. We adopted the same approach as described in FSM13 to determine the angular sizes and peak H I column density. Two-dimensional Gaussian fitting was used to derive position angle, semi-major and semi-minor axes. It uses the brightness centroid for the fit, though can be inaccurate for distorted sources (e.g., clouds with two bright structures). Caution should be applied when interpreting the derived position angle. The peak N_{HI} was determined by locating the brightest pixel in the integrated H I column density map of each source.

In Westmeier et al. (2012), tests were performed to evaluate the reliability of *Duchamp* for parametrizing sources. Artificial unresolved and extended H I sources were generated and tested with various parameters. They demonstrated that *Duchamp* is a powerful source finder with the capability of detecting sources down to low signal-to-noise ratio. However, parameters such as the integrated flux (F_{int}) measured by *Duchamp* suffer from systematic errors. The integrated flux of faint sources is underestimated by *Duchamp*. In order to correct for this systematic error, we employed the same procedures as described in FSM13 to derive the correction factor for sources in our catalog. In brief, we used the same stand-alone parametrization algorithm as employed in FSM13 to measure the integrated flux of our sources (F'_{int}). Subsequently, the ratio of measured F'_{int} to F_{int} as a function of F_{int} in various bins was fitted with a polynomial. Figure 3 shows the comparison between the functions derived in this study (blue dashed line) and FSM13 (red dotted line). Both fitted functions represent the underestimation factor for a given F_{int} and behave similarly. Either function can be used for correcting integrated fluxes measured by *Duchamp* in future work. In this paper, we adopted the function derived from sources in this catalog.

As for derived peak T_{B} and peak N_{HI} measured by *Duchamp*, corrections are not necessary, but small systematic errors of the order of 5–10% of the derived values are expected (FSM13). The velocity FWHM values measured by *Duchamp* are generally accurate (see Figure 8 of Westmeier et al. 2012).

The completeness of our catalog depends on the detection rate of *Duchamp*. Simulations to check the detection rate were performed by FSM13. Fake clouds of various input parameters were injected into the data cube at random locations and searched by *Duchamp*. They find that *Duchamp* is generally reliable for detecting clouds with narrow lines, but likely to miss clouds with faint (T_{B}=0.14–1.0 K) or broad velocity lines (velocity FWHM=16–30 km s^{-1}). The recovery rate for faint or broad velocity lines clouds is 80%. We expect the same detection rate for the present catalog.

5. Cloud Properties

In Figure 4, we show histograms of MS longitude and MS latitude in the new coordinate system, V_{GSR}, V_{LSR}, peak H I column density in logarithmic scale and velocity FWHM (from top left to bottom right). Galaxies and objects with a warning flag in the catalog are excluded in these histograms. We find that the number of HVCs decreases linearly (with coefficient of determination of 0.96) from $-20°$ to $-70°$ in L_{MS}. The low number of HVCs at $L_{\mathrm{MS}} = -10°$ is due to the incomplete sky coverage. For B_{MS}, the distribution is Gaussian with the peak at $0°$. HVCs agglomerate in a narrow B_{MS} range of $\pm 10°$. We also find a flat distribution in V_{GSR} for the GASS data. Most HVCs found in the H75GASS data are distributed between 0 and 100 km s^{-1} in the GSR velocity frame. A bimodal distribution is seen in V_{LSR}, with median of velocities -140 and $+150$ km s^{-1}. The lack of clouds in the negative V_{LSR} range is due to selection effects. The peak N_{HI} distribution is distinctly different between HVCs found in GASS and H75GASS data. Both exhibit a normal Gaussian distribution with the majority of low and high H I column density clouds being detected in GASS and H75GASS data, respectively. The lower H I column density limit in the two datasets is due to sensitivity. The gap between the histograms appears to a resolution effect – peak column densities will always be higher for the higher angular resolution H75GASS data. Although not shown here, the distribution of peak N_{HI} is uniform with respect to L_{MS}. The distribution in average column density (integrated over B_{MS}) is also uniform in the range $L_{\mathrm{MS}} = -20°$ to $-70°$. However, as shown in Figure 10 of Nidever et al. (2010), there is an exponential decrease thereafter. The FWHM velocity distribution suggests that clouds in this region have a median value of 25 km s^{-1} and their overall distribution is similar to that found in the LA region (FSM13), except that there are no HVCs with a velocity FWHM

greater than 80 km s^{-1} in the MS region.

5.1. Comparison with the P02 Catalog

The P02 HVC catalog is based on reprocessed HIPASS data, which recovers slightly more extended emission than the original HIPASS processing (see Putman et al. 2003 for details). The search for objects was performed using a friends-of-friends cloud search algorithm (de Heij et al. 2002). The P02 catalog covers the entire right ascension range, the declination range of $\delta < +2°$ and the velocity range of $-500 \leq V_{\text{LSR}} \leq +500$ km s^{-1}. Since the LSR velocity range of ± 90 km s^{-1} does not exclude all the Galactic emission, an additional constraint based on the deviation velocity ($V_{\text{dev}} > 60$ km s^{-1}), defined by Wakker (1991) to be the difference from a simple Galactic rotation model, was added by P02 to the selection criteria for their HVCs. They noted that the excluded objects may contain real HVCs with some having an appearance similar to the small-scale structure in the gaseous disk of the Milky Way.

In Figure 5, we show 253 sources in our catalog and 183 sources in P02 catalog that fall within our searched velocity and spatial volume. There are ~ 71 sources identified as being the same source in two catalogs, with the majority of them detected in the GASS data (see right panel). This suggests that most of the sources detected in the H75GASS data are unique. Comparing the rates for identifying the same P02 sources between this study and FSM13, we find them to be $\sim 40\%$ and $\sim 50\%$, respectively. Given the high brightness sensitivity of HIPASS as compared to GASS and H75GASS, P02 recovered many faint HVCs that were not detected in our dataset (e.g., the positive MS latitudes in MS IV) in Figure 5. However, there is a lack of P02 detections in the IFR due to the nature of the reprocessed HIPASS data, in which emission is filtered out in individual channels in this region. The manner in which clouds are merged or broken up can affect overlap between the catalogs. Both GASS and H75GASS have excellent spectral resolution, which allows us to resolve HVCs with narrow lines. The high-resolution H75GASS data recover a significant number of compact sources, which cannot be resolved in the lower resolution GASS and HIPASS data. This is clearly seen in the peak N_{HI} distribution (Figure 4). We show the velocity FWHM distribution of both catalogs in Figure 6. HVCs that overlap with the Galactic emission and/or lie at the spatial edge of the image and galaxies have been excluded in this plot. This figure shows that the excellent spectral resolution of GASS and H75GASS allows clouds with narrow-line components to be resolved. Most of the HVCs in our and the P02 catalog have velocity FWHM of 15–25 km s^{-1} and 35–45 km s^{-1}, respectively. While few in number, our catalog does contain HVCs with large velocity FWHM (> 40 km s^{-1}).

6. H I GAS AND KINEMATIC DISTRIBUTION

The Magellanic Stream has traditionally been viewed as consisting of six main concentrations (e.g., Mathewson et al. 1974). Subsequent observations with higher sensitivity revealed its complexity (see e.g., Cohen 1982; Putman et al. 2003; Brüns et al. 2005; Nidever et al. 2008). Two distinct filaments were recovered, which run alongside each other with no clear starting point but appeared to be connected to the IFR (Brüns et al. 2005). Brüns et al. (2005) defined a separation between the IFR and start of the MS near $l = 300°$ and $b = -61°$. Nidever et al. (2008) studied the MS and LA using a Gaussian decomposition method on the LAB data and claimed to trace one of the MS filaments back to the southeast H I overdensity region of the LMC. In this section, we use both the H75GASS and GASS data (complementary to each other) to revisit the overall morphology and kinematics of the MS, and to discuss the detailed morphology of filaments and HVCs in the MS.

6.1. The overall morphology

In Figures 1 and 2, we show the integrated H I column density maps of H75GASS and GASS data with nomenclature for various parts of the MS. In contrast to the study by Brüns et al. (2005), careful examination reveals that the two filaments of the MS are actually extended into the IFR, this redefining the starting point of the MS. This continuity is also observed in the LAB data studied by Nidever et al. (2008). They showed that both filaments are running parallel at the head of the stream.

To trace the two filaments at the head of the stream, we use the GASS data, which has a better angular resolution than the LAB data. Figure 7 shows the area of investigation, which covers the SMC, LMC and the head of the MS. The dual-filaments are also labeled as filament 1 and 2. Series of channel maps in the V_{LSR} range from +180 to +275 km s^{-1}, with an interval of $\sim$4 km s^{-1}, are shown in Figures 8 and 9. Tracing the most prominent filament (namely filament 1, indicated by black arrow) from velocity channels between +180 and +201 km s^{-1}, we find that it extends toward the SMC. A connection to the SMC emerges at +201 km s^{-1} and extends into the the northern end of the Magellanic Bridge (second black arrow as shown in +205 km s^{-1} channel map), where H I gas from the SMC is dominant. The exact ending point of filament 1 is ambigious as it eventually mixes in with the Magellanic Bridge emission. In Figure 7, we show the channel map at +201 km s^{-1}in which distinct gaps are indicated. Gaps are common along the MS. Examining the channel maps beyond +255 km s^{-1}, we find that the gas from the LMC is dominant and eventually a distinct sinusoidal pattern emerges from the Arm B of LMC (see the last channel map of Figure 9). This gaseous feature appears isolated and does not seem to connect to the filament 1. The

exact starting point of filament 2 is hard to trace but the overall structure appears to be connected to the Magellanic Bridge through SMC (indicated by green arrow).

These two filaments appear to be widely separated at the head of the stream and become thinner and have decreasing H I column density from the head to tail of the stream. They eventually turn into a clumpy filamentary structure, which is not shown in this study but revealed in the studies by Stanimirović et al. (2008) and Nidever et al. (2010). They also appear to be twisted several times along the stream, in a double-helical structure (Putman et al. 2003).

We present the velocity field of the H75GASS and GASS data in V_{LSR} in Figure 10 and V_{GSR} in Figure 11. The maps show that the observed MS covers a large velocity range, $-250 \lesssim V_{\mathrm{LSR}} \lesssim +250$ km s^{-1} and $-200 \lesssim V_{\mathrm{GSR}} \lesssim +200$ km s^{-1}. Faint and thin filamentary structures are not visible in these maps due to noise clipping but are visible in the integrated H I column density maps (Figure 1 and 2). While it is hard to disentangle the bifurcated feature spatially in the integrated H I column density map, the velocity field map provides a powerful tool to trace the filaments. The head of the stream starts at positive velocity and trails at negative velocity. The transition between the positive and negative velocity occurs near $(L_{\mathrm{MS}}, B_{\mathrm{MS}}) = -50°,0°$ (i.e., MS II). This part of the stream is difficult to analyze because it extends across 0 km s^{-1} and crosses in front of the Sculptor Group galaxies that have velocities ranging from 50 to 700 km s^{-1} (Putman et al. 2003). Contamination from the Galactic emission depends on the selected velocity channels (see § 3.1).

While the velocity gradient is clearly seen along the stream, a $V_{\mathrm{LSR}}=5.6$ km s^{-1}deg^{-1} transverse velocity gradient, in the sense that velocity decreases as a function of increasing declination, near $L_{\mathrm{MS}} = -50°$, was pointed out in Cohen (1982). The exact gradient is difficult to measure using HIPASS due to low spectral resolution (Putman et al. 2003). Examining the high spectral resolution of GASS and H75GASS data, we do not find such transverse velocity gradient in the specified region ($L_{\mathrm{MS}} \sim -50°$). However, we should point out that the structure in this region is contaminated by the Galactic emission. Proper subtraction of the Galactic emission is needed to further investigate the existence of the transverse velocity gradient in this particular region. Nevertheless, if we examine the position-velocity map in declination of the entire observed MS (Matthews et al. 2014), a transverse velocity gradient of 6.4 km s^{-1}deg^{-1} in the GSR velocity is evident.

6.2. HVCs in the Magellanic Stream

We have shown the on-sky distribution of HVCs found in the region of the MS in §5.1 (see Figure 5). The most noticeable pattern is the overabundance of HVCs near the South Galactic Pole (SGP) (right panel of Figure 5). HVCs in this region partially overlap in $V_{\rm LSR}$ with the Sculptor Group of galaxies. The coincidence between these clouds and the Sculptor Group galaxies was first pointed out by Mathewson et al. (1975). Putman et al. (2003) carried out a comprehensive analysis and discussion regarding the origin of these clouds. Their conclusion is that these clouds are unlikely to be members of the Sculptor Group due to their velocity and spatial distributions not being much different from the bulk of Stream clouds.

Distinguishing between genuine HVCs associated with the MS and Sculptor Group is not easy based on the velocity information alone. Sculptor Group galaxies have a higher H I column density. But HVCs in the MS are hard to distinguish from intrinsically large HVCs or tidal debris in the Sculptor Group if they exist. We find that HVCs with large differences in velocity and H I column density from the two filaments exist everywhere along the stream. Figure 12 shows the distribution of clouds in the $L_{\rm MS}$ – $V_{\rm LSR}$ plane. It shows that the overabundance of HVCs is not unique to the South Galactic Pole. Large numbers of cloud are also found in the IFR ($L_{\rm MS} \sim -20°$ to $-30°$). These were not seen by Putman et al. (2003) due to resolution and artifacts in the HIPASS data. Therefore, the overabundance of clouds in the SGP region is even less significant than before.

To probe the interaction between the MS and the ambient halo medium, it is useful to study the morphology of the HVCs. Here we classify the HVCs in our catalog based on the morphological classification scheme of FSM13: (1) clouds with head-tail structure and velocity gradient (HT); (2) clouds with head-tail structure but without velocity gradient (:HT); (3) bow-shock shaped clouds (B); (4) symmetric clouds (S); and (5) irregular/complex clouds (IC).

Among these groups, head-tail clouds are particularly interesting because their compressed head with a diffuse tail provides direct evidence of gas being stripped from the main condensation due to interaction with the surrounding ambient gas. Besides the traditional cometary structure, head-tail clouds also come in many other varieties. For example, they may contain additional clump of diffuse gas, or have a kink in the tail or velocity gradient that is generally associated with the H I column density gradient. It is also known that head-tail clouds with a velocity gradient consist of two subgroups: those with the velocity of the head either leading (pHT) or lagging (nHT) tail (Putman et al. 2011; FSM13). We omit head-tail clouds that do not resemble the obvious cometary like structure due to different viewing angles in this study (see e.g., Plöckinger & Hensler 2012).

We find no obvious differences in the distributions among group 1, 2 and subgroup of pHT and nHT, and hence, analyze them all together here. In Figure 13, we show the on-sky $V_{\rm LSR}$ distribution of head-tail clouds with and without velocity gradient in the region of the MS. Their distributions in $L_{\rm MS}$ and $B_{\rm MS}$ are shown in Figure 14. Head-tail clouds found in H75GASS data are generally compact and high in H I column density. For their distribution in $V_{\rm LSR}$, the head-tail clouds in general follow the velocity gradient along the stream. Few head-tail clouds have large $V_{\rm LSR}$ difference (100–200 km s^{-1}) from the $V_{\rm LSR}$ of the nearby filaments. This is most obvious near the SGP (or MS II) and IFR. Most head-tail clouds are at $-60° \lesssim L_{\rm MS} \lesssim -20°$ and $-5° \lesssim B_{\rm MS} \lesssim +10°$. Compared to the distribution of all HVCs in $B_{\rm MS}$ (Figure 4), most of the clouds at $B_{\rm MS} \sim 10°$ are head-tail clouds.

The pointing direction of the head-tail clouds is also shown in Figure 13, with head and tail being enlarged for better visibility. Due to the measurement errors in position angle, in some cases we manually inspected the cloud and adjusted the values whenever necessary to better represent the pointing direction of the clouds (as discussed in FSH13). In Figure 15, we show the histogram of the pointing direction of the head-tail clouds. There is no preferential pointing direction but careful examination reveals a nearly equal number pointing either toward (225°–315°) or away (45°–135°) from the head of the stream. We also find a total number of 70 head-tail clouds, which is $\sim 28\%$ of all HVCs in our catalog. 60% (42/70) of the head-tail clouds show a clear velocity gradient, with a nearly equal number of clouds for the velocity gradient subgroups, i.e., 20 vs 21 for nHT and pHT, respectively. The percentages are very similar to those found in the LA region (FSM13). We have about a factor of six more head-tail clouds in this study than the study by Putman et al. (2011) in the same region. This may partly be due to different selection criteria. While the LA region still has a factor of 1.5 more head-tail clouds than the MS region, this finding is unexpected because disturbed clouds are absent in MS VI (Stanimirović et al. 2008). We will discuss the implication of the pointing direction and large number of head-tail clouds in the MS in § 7.

The bow-shock-shaped clouds have a similar morphological structure to the head-tail clouds. They are characterized by a compressed head but with two deflected gas wings instead of a tail. Many studies suggest that bow-shock-shaped cloud are less common than head-tail clouds despite both of them showing evidence of ram-pressure interaction with the ambient medium (see e.g., Westmeier et al. 2005; FSM13). On the other hand, symmetric clouds morphologically do not show signs of disturbance, although head-tail cloud pointed directly along the line of sight can appear as a symmetric cloud. The total numbers of bow-shock-shaped and symmetric clouds are 8 and 35 in our catalog, respectively. This is about half the number of symmetric clouds in the MS as compared to the LA region. Figure 17 shows the distributions of bow-shock-shaped (diamonds and crosses) and symmetric clouds

(hexagons and triangles) in V_{LSR}. Distributions of symmetric clouds in L_{MS} and B_{MS} are shown in Figure 16. They are distributed evenly across the entire range of L_{MS}, but mainly populate the range of $\sim 0°–5°$ in B_{MS}. The V_{LSR} distribution is quite similar to the one for head-tail clouds. Velocity gradients are common among the symmetric clouds. One notable, distinctive bow-shock-shaped cloud is HVC+73.7−67.5−213, which is located in MS IV. It is a relatively large $(1.2°)$ compared to others found in this study.

7. Discussion

The formation of the MS has previously been attributed to either tidal or ram-pressure mechanisms. Many efforts have been put into creating tidal models that accurately reproduce the global morphology such as the bifurcation of the MS. However, these tidal models fail to reproduce some of the observed features, such as the gradual decrease in H I column density along the stream. Ram-pressure models, on the other hand, are able to help overcome this problem. Thus, the formation of the MS might be due to a combination of ram-pressure and tidal stripping. Implementing both formation mechanisms simultaneously into simulations is not an easy task due to the large number of particles required to resolve the ISM and hot gas interaction. A notable attempt to employ both physical mechanisms is the study of Mastropietro et al. (2005). The drawback of their model is the sole consideration of 2-body tidal interaction (MW-LMC), whereas in many tidal models, the SMC plays an important role in the formation of the MS. Metallicity measurements of *FUSE* and *HST* spectra suggest that most of the MS originates from the SMC (Sembach et al. 2001; Fox et al. 2010, 2013). In this section, we mainly discuss the effect of ram-pressure stripping on the MS.

Aspects such as overall morphology and decrease in H I column density of the two filaments can be explained by the ram-pressure model and evaporation of gas clouds. Models of ram pressure stripped galaxies (viewed edge-on) have shown that ram-pressure is sufficient to remove part of the neutral gas from the disk (Mastropietro et al. 2005). The stripped gas trails behind the galaxy, and the morphology at early times looks like a bow shock (see e.g., Figure 4 of Mastropietro et al. 2005). As the interaction time continues, the gas in the disk decreases significantly. Eventually, islands of complex filaments are formed in the trailing direction and fan out near the end (Steinhauser et al. 2012), which is morphologically similar to the MS that we see today (Stanimirović et al. 2008). Clouds that are stripped first would have longer interaction time with the hot halo and sustain larger loss of gas due to evaporation.

To further investigate the effect of ram-pressure on a smaller scale, we examine the distributions of head-tail clouds and their pointing direction. These head-tail clouds are

presumably the debris of larger filaments broken off due to ram-pressure stripping. Thus, they are expected to follow the motion of the larger filaments, i.e., with their head pointing toward the SMC and their tail pointing in the direction of decreasing L_{MS}. However, they seem to be pointing in a random direction, similar to the finding in the LA region (FSM13). This is a rather surprising result because the random motion of head-tail clouds in the region of the LA is presumably caused by strong turbulence generated from the collision between the LA and the Galactic disk gas. This scenario of incoming warm neutral gas colliding with the hotter ambient medium (Audit & Hennebelle 2005) is inadequate to explain the random pointing of head-tail clouds in the MS region, even though turbulence must be at play as well. We look into the cascade scenario, which was originally proposed to explain the observed Hα emission along the MS (Bland-Hawthorn et al. 2007). In the hydrodynamical simulation of Bland-Hawthorn et al. (2007), the upstream clouds experience gas depletion via Kelvin-Helmholtz (KH) instability due to interaction with the hot halo. The depleted gas plows into the following cloud, which leads to shock ionization and depletion of the downstream clouds. The entire process continues downstream like a chain-reaction. During this process, the downstream clouds transfer momentum to the depleted gas in the front, which results in Rayleigh-Taylor (RT) instabilities. With both KH and RT instabilities, the process becomes highly turbulent for the entire region. This scenario agrees with the observational properties of head-tail clouds in the MS.

The life time of the disrupted clouds in the cascade scenario is 100–200 Myr, which is relatively short as compared to the age of the stream (1–2 Gyr) as estimated from simulations. Constant replenishment of gas from the MCs is needed to reproduce the observed structure (Bland-Hawthorn et al. 2007). Other physical parameters can also lengthen the lifetime and govern the stability of clouds, for example, magnetic field, dark-matter, heat conduction, size and, halo and cloud densities. Two and/or three-dimensional hydrodynamical simulations have experimented with these parameters (see e.g., Quilis & Moore 2001; Plöckinger & Hensler 2012; Heitsch & Putman 2009; Vieser & Hensler 2007).

In Quilis & Moore (2001), the behavior of pure gas clouds and dark-matter dominated HVCs interacting with the different halo environment was investigated. They found that head-tail structures emerge when the ambient environment reaches a density of 10^{-4} cm^{-3} with a cloud velocity of 200 km s^{-1}. HVCs with a dark-matter component survive longer (~ 10 Gyr) as compared to those without (~ 10 Myr). However, the same cloud was not tested with and without dark-matter. The recent Plöckinger & Hensler (2012) models considered this effect and found that dark-matter free HVCs can easily survive for 100 Myr. Their model also suggests that dark-matter free clouds are physically much similar to the observed large HVC complexes with a heterogeneous multi-phase internal gas structure.

The effect of heat conduction for stabilizing the HVCs (or Giant Molecular Clouds) is explored by Vieser & Hensler (2007). Their models show that clouds with two-phase structure can stabilize and survive longer as a result of heat conduction. While heat conduction may explain the longer survival timescale of head-tail clouds in the MS, massive clouds like the filaments of the MS are yet to be tested in simulations (G. Hensler, priv. comm.). Heitsch & Putman (2009) also explored effects of various physical parameters based on two experimental setups: wind-tunnel and free-fall. Their results show that clouds with H I masses less than $10^{4.5}$ $M_\odot$ will lose their gas after moving only 10 kpc or less under typical halo density and relative velocity conditions. The visibility of the head-tail structure depends on the viewing angle. Nevertheless, all the hydrodynamical simulations have so far only considered clouds at lower z (distance from the Galactic plane) due to the large uncertainty in the halo density beyond 10 kpc. This implies that these models might not be suitable for explaining the evolution of HVCs originating from the MCs. Interestingly, HVCs created with these models are morphologically and physically similar to what we observe, e.g., the bow-shock-shaped cloud, HVC+73.7−67.5−213, and the head-tail clouds.

There is an overall larger number of head-tail clouds in the MS region found in this study as compared to the study by Putman et al. (2011) (see §6.2). It is possible that we missed some of the head-tail clouds not resembling classical head-tail morphologies due to different viewing angles (see Plöckinger & Hensler 2012), which will increase the number of head-tail clouds. While a larger number of head-tail clouds is found, there is a significant decrease in number toward the tail end ($L_{MS} > -60°$; see the left panel of Figure 14). This is consistent with the finding of a lack of head-tail clouds in the region of MS IV (Stanimirović et al. 2008), which suggests that ram-pressure stripping has less of an effect on the tail end of the stream. This is not surprising given that the predicted model distance is the largest at the tail end of the stream, which the ram-pressure decreases as a function of distance square in an assumed isothermal halo model. It is also possible that the tail of the MS is aligned radially along the line-of-sight (see Figure 4 of Diaz & Bekki 2012), in which case viewing geometry would reveal more symmetric cloud shapes.

We find that the number of symmetric clouds is about a factor of two smaller than the number of head-tail clouds in the range $-60° < L_{MS} < -20°$. A slight increase in the number of symmetric clouds as compared to head-tail clouds is observed beyond $L_{MS} \sim -60°$. We know that the MS VI region is exclusively populated with symmetric clouds (Stanimirović et al. 2008). This raises the question whether we will see a continual trend of increasing number of symmetric clouds in the MS V region, which is outside our currently studied area. If the answer is yes, then this would further confirm the model prediction of distance increasing as a function of L_{MS}. With this in mind, it is rather puzzling to see that the northern extension of the stream (Nidever et al. 2010) has a very different morphology

from other parts of the MS. It morphologically looks more like the LA (FSM13). A statistical analysis of different morphological types of HVCs in the northern extension might shed some light on the distance scale of the farthest end of the stream.

8.   Summary and Conclusions

We have compiled a catalog of HVCs in the Magellanic Stream using new ATCA and Parkes (GASS) data. The catalog includes 251 HVCs and 2 galaxies. Most of the clouds detected in the combined H75GASS are unique. We used *Duchamp* as a source finding tool and to parametrize the detected sources. Most of the parameters were derived from *Duchamp* except the angular size and the peak H I column density, which were determined independently. We made a comparison between our catalog and Putman et al. (2002), who employed the reprocessed HIPASS data for their study.

We have presented the distributions of clouds and their properties. The HVCs agglomerate in a narrow Magellanic Stream latitude (B_{MS}) range of $\pm10°$ and decrease linearly with decreasing Magellanic Stream longitude (L_{MS}). The kinematics show bimodality in V_{LSR} but none in V_{GSR}. The majority of the clouds detected in GASS have lower H I column density than in H75GASS. The overall velocity FWHM distribution is similar to that found in the Leading Arm region (FSM13).

The overall morphology and kinematics of the MS have been revisited. We find that the two filaments of the MS are extended into the IFR, connected to the SMC and extend into the northern end of the Magellanic Bridge. The former finding is consistent with the study by Nidever et al. (2008), but differs from the conclusion of Brüns et al. (2005). The connection to the SMC and Magellanic Bridge is contradictory to the conclusions of Nidever et al. (2008). Our suggestion that the two filaments of the MS are twisted and largely emanate from the SMC is consistent with the Fox et al. (2013) metallicity measurements, which show 0.1 solar metallicity along much of the Stream. While we could not investigate the existence of the transverse velocity gradient as seen in Cohen (1982) in this study, we found a clear transverse velocity gradient of 6.4 km s^{-1}deg^{-1} in the GSR velocity frame based on the position-velocity map of Matthews et al. (2014).

We find that the MS has a complex filamentary structure. Morphological classification is presented and distributions of each type are discussed. In contrast to the studies by Stanimirović et al. (2008) and Putman et al. (2011), we found a large number of head-tail clouds in the MS region. This strongly suggests that ram-pressure stripping plays an important role in the formation mechanism of the MS. The pointing direction of the head-tail

clouds appear to be random, which suggests the presence of strong turbulence. The turbulence induced by the cascade scenario is a likely cause. We also discussed various physical parameters that can lengthen the lifetime of the HVCs. While hydrodynamical simulations of HVC may not explain the HVCs origin from the MCs, they do show how small scale structure may arise. Evaporation of gas clouds is also responsible for the decrease of H I column density as seen toward the tail end of the MS.

REFERENCES

Audit, E. & Hennebelle, P. 2005, A&A, 433, 1

Barnes, D. G., Staveley-Smith, L., de Blok, W. J. G., Oosterloo, T., Stewart, I. M., Wright, A. E., Banks, G. D., Bhathal, R., Boyce, P. J., Calabretta, M. R., Disney, M. J., Drinkwater, M. J., Ekers, R. D., Freeman, K. C., Gibson, B. K., Green, A. J., Haynes, R. F., te Lintel Hekkert, P., Henning, P. A., Jerjen, H., Juraszek, S., Kesteven, M. J., Kilborn, V. A., Knezek, P. M., Koribalski, B., Kraan-Korteweg, R. C., Malin, D. F., Marquarding, M., Minchin, R. F., Mould, J. R., Price, R. M., Putman, M. E., Ryder, S. D., Sadler, E. M., Schröder, A., Stootman, F., Webster, R. L., Wilson, W. E., & Ye, T. 2001, MNRAS, 322, 486

Besla, G., Kallivayalil, N., Hernquist, L., Robertson, B., Cox, T. J., van der Marel, R. P., & Alcock, C. 2007, ApJ, 668, 949

Besla, G., Kallivayalil, N., Hernquist, L., van der Marel, R. P., Cox, T. J., & Kereš, D. 2012, MNRAS, 421, 2109

Bland-Hawthorn, J., Sutherland, R., Agertz, O., & Moore, B. 2007, ApJ, 670, L109

Braun, R. & Burton, W. B. 1999, A&A, 341, 437

Brüns, C., Kerp, J., Staveley-Smith, L., Mebold, U., Putman, M. E., Haynes, R. F., Kalberla, P. M. W., Muller, E., & Filipovic, M. D. 2005, A&A, 432, 45

Cohen, R. J. 1982, MNRAS, 199, 281

Connors, T. W., Kawata, D., & Gibson, B. K. 2006, MNRAS, 371, 108

de Heij, V., Braun, R., & Burton, W. B. 2002, A&A, 391, 159

Diaz, J. & Bekki, K. 2011, PASA, 28, 117

Diaz, J. D. & Bekki, K. 2012, ApJ, 750, 36

For, B.-Q., Staveley-Smith, L., & McClure-Griffiths, N. M. 2013, ApJ, 764, 74

Fox, A. J., Richter, P., Wakker, B. P., Lehner, N., Howk, J. C., Ben Bekhti, N., Bland-Hawthorn, J., & Lucas, S. 2013, ArXiv e-prints

Fox, A. J., Wakker, B. P., Smoker, J. V., Richter, P., Savage, B. D., & Sembach, K. R. 2010, ApJ, 718, 1046

Gardiner, L. T. & Noguchi, M. 1996, MNRAS, 278, 191

Gibson, B. K., Giroux, M. L., Penton, S. V., Putman, M. E., Stocke, J. T., & Shull, J. M. 2000, AJ, 120, 1830

Heitsch, F. & Putman, M. E. 2009, ApJ, 698, 1485

Kalberla, P. M. W., Burton, W. B., Hartmann, D., Arnal, E. M., Bajaja, E., Morras, R., & Pöppel, W. G. L. 2005, A&A, 440, 775

Kalberla, P. M. W., McClure-Griffiths, N. M., Pisano, D. J., Calabretta, M. R., Ford, H. A., Lockman, F. J., Staveley-Smith, L., Kerp, J., Winkel, B., Murphy, T., & Newton-McGee, K. 2010, A&A, 521, A17

Kallivayalil, N., van der Marel, R. P., & Alcock, C. 2006a, ApJ, 652, 1213

Kallivayalil, N., van der Marel, R. P., Alcock, C., Axelrod, T., Cook, K. H., Drake, A. J., & Geha, M. 2006b, ApJ, 638, 772

Kallivayalil, N., van der Marel, R. P., Besla, G., Anderson, J., & Alcock, C. 2013, ApJ, 764, 161

Lu, L., Sargent, W. L. W., Savage, B. D., Wakker, B. P., Sembach, K. R., & Oosterloo, T. A. 1998, AJ, 115, 162

Lu, L., Savage, B. D., & Sembach, K. R. 1994, ApJ, 437, L119

Mastropietro, C., Moore, B., Mayer, L., Wadsley, J., & Stadel, J. 2005, MNRAS, 363, 509

Mathewson, D. S., Cleary, M. N., & Murray, J. D. 1974, ApJ, 190, 291

—. 1975, ApJ, 195, L97

Matthews, D., Staveley-Smith, L., For, B.-Q., Dyson, P., Muller, E., & McClure-Griffiths, N. 2014, ApJ, in prep

McClure-Griffiths, N. M., Pisano, D. J., Calabretta, M. R., Ford, H. A., Lockman, F. J., Staveley-Smith, L., Kalberla, P. M. W., Bailin, J., Dedes, L., Janowiecki, S., Gibson, B. K., Murphy, T., Nakanishi, H., & Newton-McGee, K. 2009, ApJS, 181, 398

McGee, R. X. & Newton, L. M. 1986, Proceedings of the Astronomical Society of Australia, 6, 471

Moore, B. & Davis, M. 1994, MNRAS, 270, 209

Nidever, D. L., Majewski, S. R., & Burton, W. B. 2008, ApJ, 679, 432

Nidever, D. L., Majewski, S. R., Butler Burton, W., & Nigra, L. 2010, ApJ, 723, 1618

Plöckinger, S. & Hensler, G. 2012, A&A, 547, A43

Putman, M. E., de Heij, V., Staveley-Smith, L., Braun, R., Freeman, K. C., Gibson, B. K., Burton, W. B., Barnes, D. G., Banks, G. D., Bhathal, R., de Blok, W. J. G., Boyce, P. J., Disney, M. J., Drinkwater, M. J., Ekers, R. D., Henning, P. A., Jerjen, H., Kilborn, V. A., Knezek, P. M., Koribalski, B., Malin, D. F., Marquarding, M., Minchin, R. F., Mould, J. R., Oosterloo, T., Price, R. M., Ryder, S. D., Sadler, E. M., Stewart, I., Stootman, F., Webster, R. L., & Wright, A. E. 2002, AJ, 123, 873

Putman, M. E., Gibson, B. K., Staveley-Smith, L., Banks, G., Barnes, D. G., Bhatal, R., Disney, M. J., Ekers, R. D., Freeman, K. C., Haynes, R. F., Henning, P., Jerjen, H., Kilborn, V., Koribalski, B., Knezek, P., Malin, D. F., Mould, J. R., Oosterloo, T., Price, R. M., Ryder, S. D., Sadler, E. M., Stewart, I., Stootman, F., Vaile, R. A., Webster, R. L., & Wright, A. E. 1998, Nature, 394, 752

Putman, M. E., Saul, D. R., & Mets, E. 2011, MNRAS, 418, 1575

Putman, M. E., Staveley-Smith, L., Freeman, K. C., Gibson, B. K., & Barnes, D. G. 2003, ApJ, 586, 170

Quilis, V. & Moore, B. 2001, ApJ, 555, L95

Richter, P., Fox, A. J., Wakker, B. P., Lehner, N., Howk, J. C., Bland-Hawthorn, J., Ben Bekhti, N., & Fechner, C. 2013, ApJ, 772, 111

Sembach, K. R., Howk, J. C., Savage, B. D., & Shull, J. M. 2001, AJ, 121, 992

Shattow, G. & Loeb, A. 2009, MNRAS, 392, L21

Stanimirović, S., Hoffman, S., Heiles, C., Douglas, K. A., Putman, M., & Peek, J. E. G. 2008, ApJ, 680, 276

Staveley-Smith, L., Kim, S., Calabretta, M. R., Haynes, R. F., & Kesteven, M. J. 2003, MNRAS, 339, 87

Steinhauser, D., Haider, M., Kapferer, W., & Schindler, S. 2012, A&A, 544, A54

van der Marel, R. P., Alves, D. R., Hardy, E., & Suntzeff, N. B. 2002, AJ, 124, 2639

Venzmer, M. S., Kerp, J., & Kalberla, P. M. W. 2012, A&A, 547, A12

Vieser, W. & Hensler, G. 2007, A&A, 472, 141

Wakker, B. P. 1991, A&A, 250, 499

—. 2001, ApJS, 136, 463

Wannier, P. & Wrixon, G. T. 1972, ApJ, 173, L119

Westmeier, T., Brüns, C., & Kerp, J. 2005, A&A, 432, 937

Westmeier, T. & Koribalski, B. S. 2008, MNRAS, 388, L29

Westmeier, T., Popping, A., & Serra, P. 2012, PASA, 29, 276

Whiting, M. T. 2012, MNRAS, 421, 3242
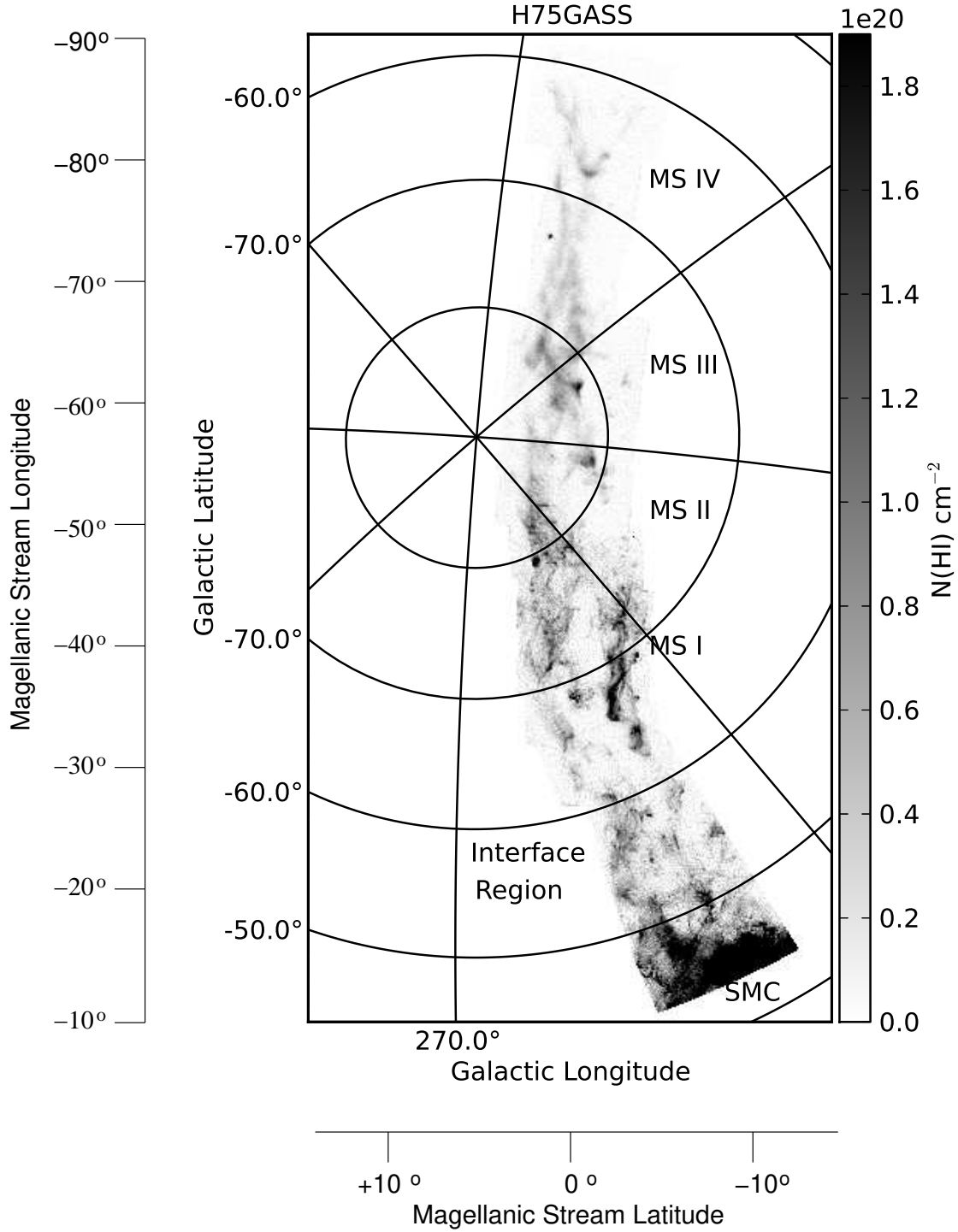
Fig. 1.— Integrated H I column density map of H75GASS for positive and negative velocities. The H I column density ranges from 0 to 1.9×10^{20} cm^{-2}. The locations of the Small Magellanic Cloud, the Interface Region and MS I–IV are labeled.
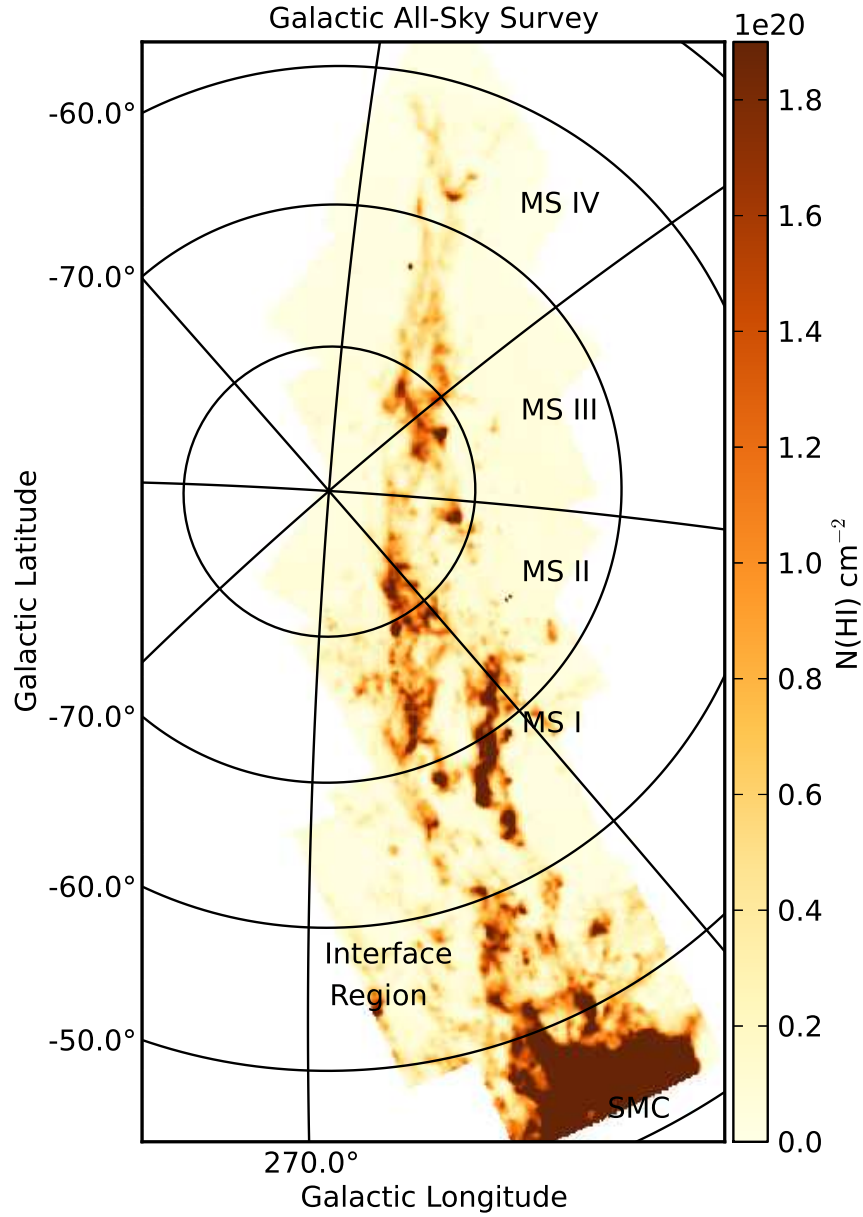
Fig. 2.— Same as Figure 1 but for the GASS data only. A slightly larger region than H75GASS is used in this study. A different color scheme is used to distinguish the two data sets.
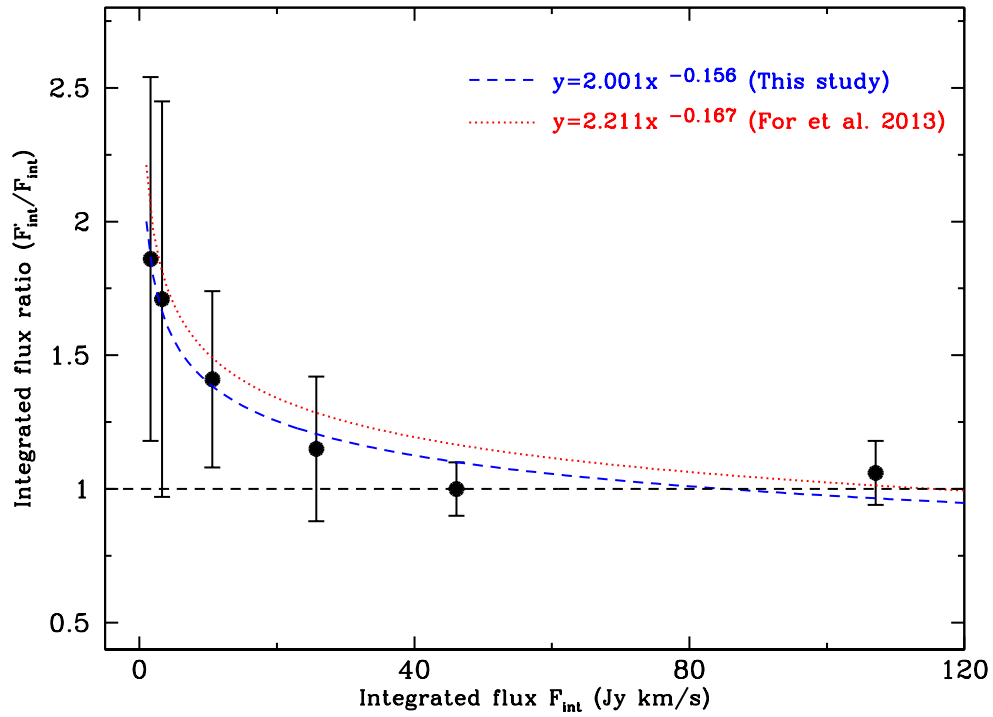
Fig. 3.— Ratio of true integrated flux (F'_{int}) to integrated flux (F_{int}) measured by *Duchamp* as a function of F_{int}. The red dotted and blue dashed lines are the fitting functions derived in For et al. (2013) and this study, respectively. They represent an estimate of the correction factor to be applied to *Duchamp* fluxes.
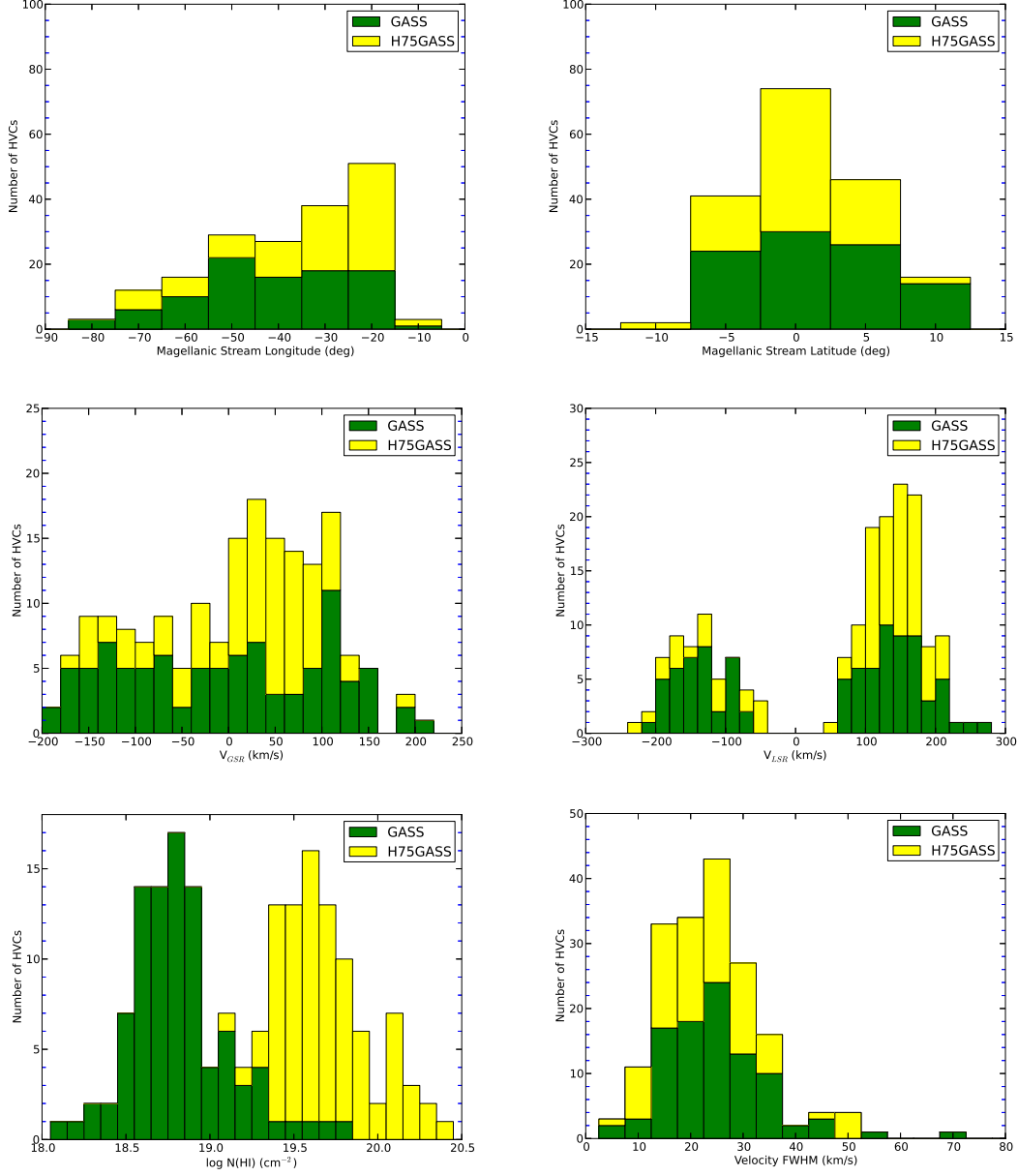
Fig. 4.— Stacked histograms of L_{MS}, B_{MS}, V_{GSR}, V_{LSR}, peak H I column density on a logarithm scale and velocity FWHM of HVCs identified in GASS (green) and H75GASS (yellow), from top left to bottom right, respectively. Excluded from the plots are galaxies and 75 HVCs that either overlap with the Galactic emission channels and/or lie at the spatial edge of the image.
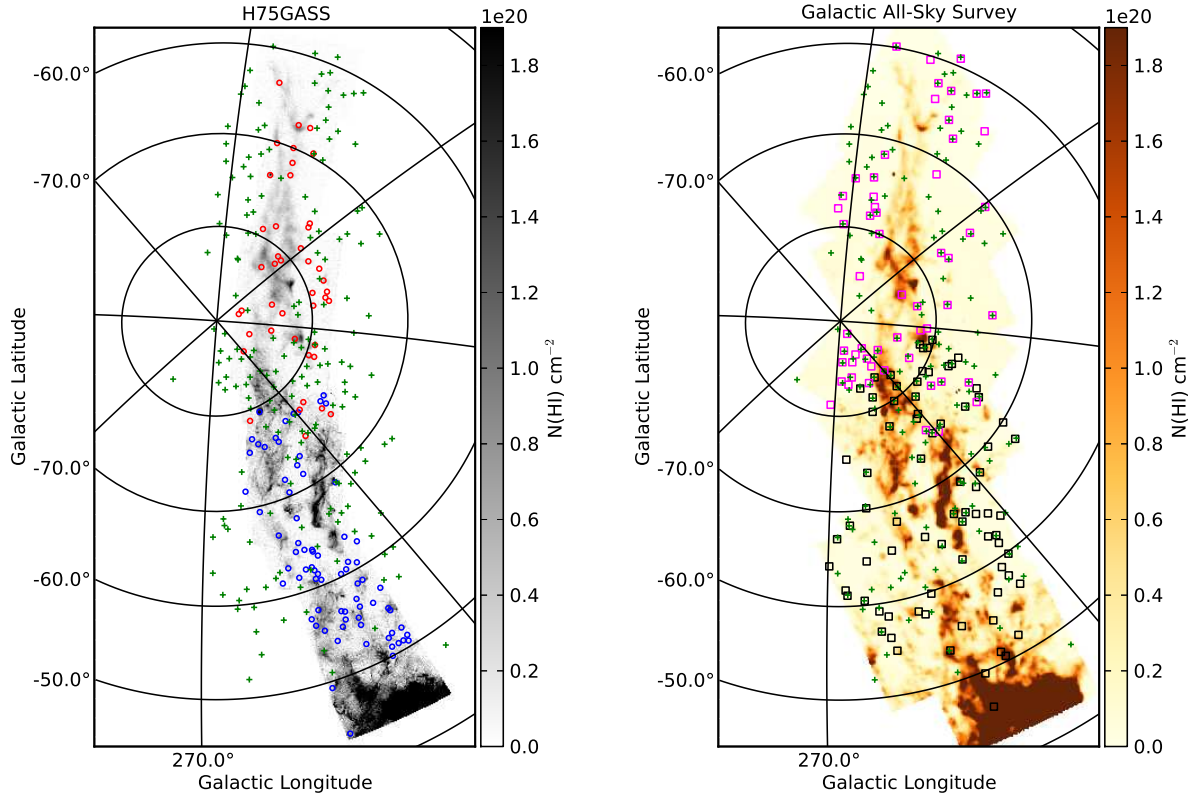
Fig. 5.— *Left*: All 118 sources detected by *Duchamp* with the H75GASS data (red and blue circles) and 183 sources detected by Putman et al. (2002) (green pluses) are overlaid onto the integrated H I column density map of H75GASS as shown in Figure 1. The blue and red circles represent *Duchamp* detections at positive and negative LSR velocities, respectively. *Right*: Same as left figure, except 135 sources detected by *Duchamp* are from GASS data and are overlaid onto the H I column density map of GASS as shown in Figure 2. The black and magenta squares represent *Duchamp* detections at positive and negative LSR velocities, respectively. The sources from Putman et al. (2002) are within the same V_{LSR} range and the same region on the sky as our GASS data presented in this paper.
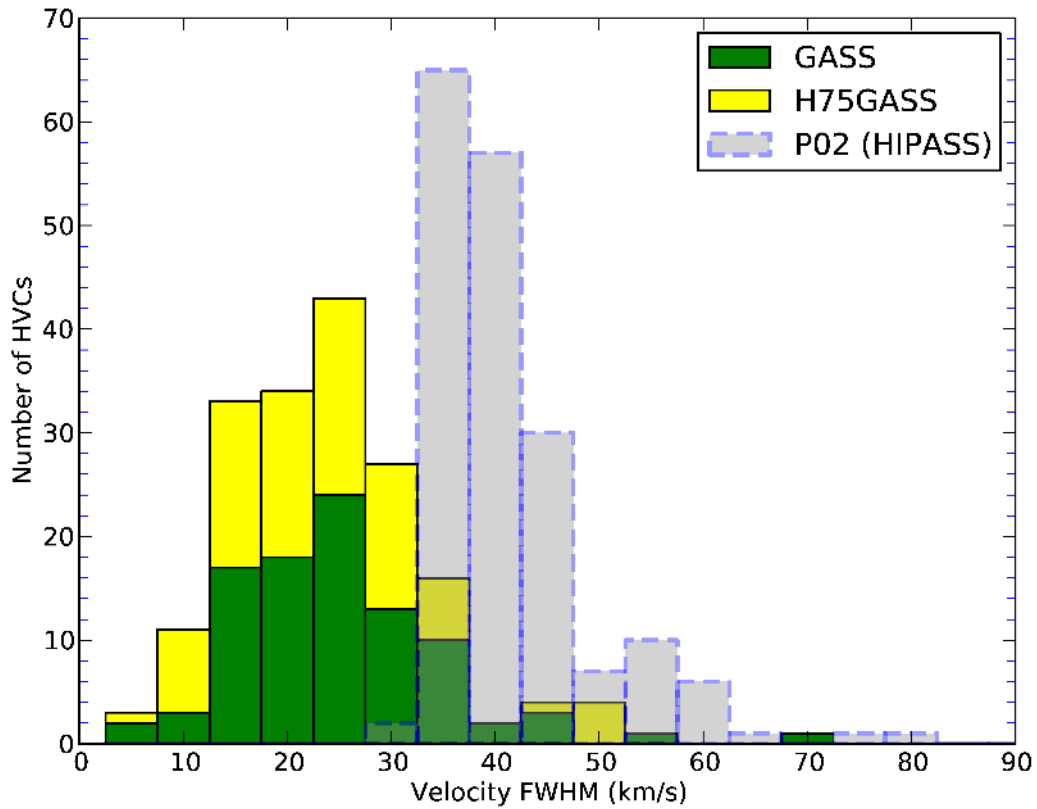
Fig. 6.— Histograms of velocity FWHM of HVCs in this study (green and yellow) and P02 (grey). Excluded from the plots are galaxies and 75 HVCs that either overlap with the Galactic emission channels and/or lie at the spatial edge of the image. Clouds with narrow lines are recovered in this study thanks to the higher spectral resolution of GASS and H75GASS as compared to HIPASS.
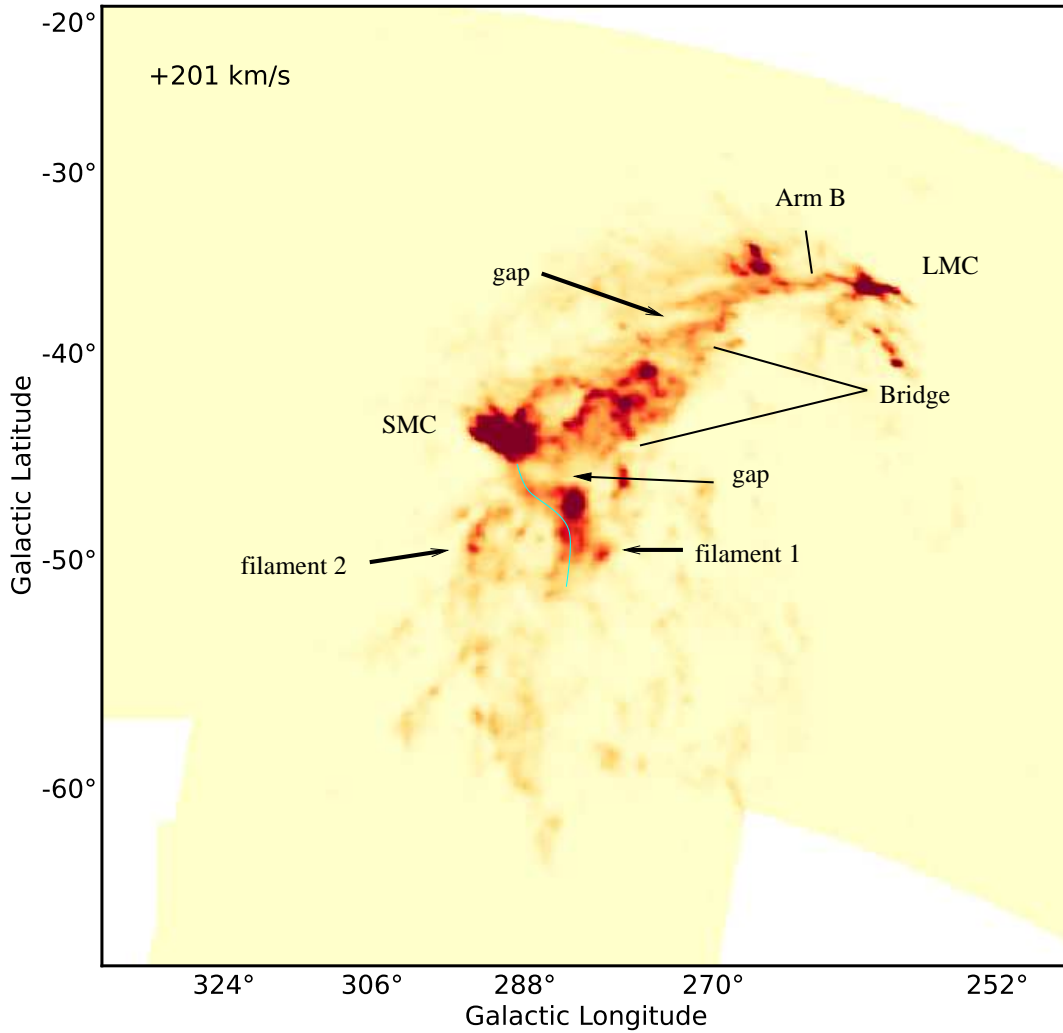
Fig. 7.— Channel map at $+201$ km s^{-1}. The Small Magellanic Cloud, Large Magellanic Cloud, Magellanic Bridge, the dual-filaments at the head of the MS and Arm B are labeled. The gaps show filament 1 is not connected to the LMC. The cyan line marks the position of filament 1 which appears to be connected to the SMC both spatially and kinematically.
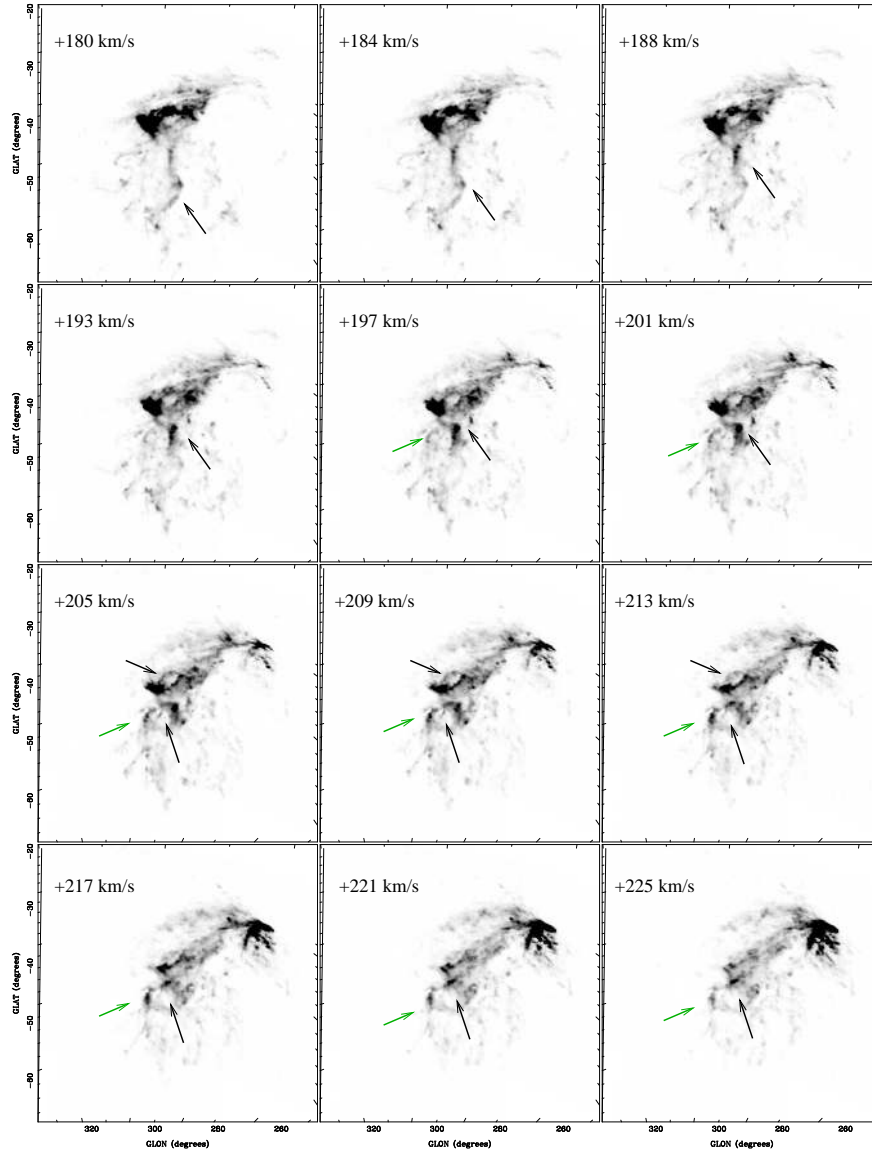
Fig. 8.— Channel maps of GASS data cube from LSR velocity of $+180$ km s^{-1} to $+225$ km s^{-1}. These maps cover the area where Small Magellanic Cloud, Large Magellanic Cloud and the head of the MS are located. Black and green arrows indicate filament 1 and 2, respectively.
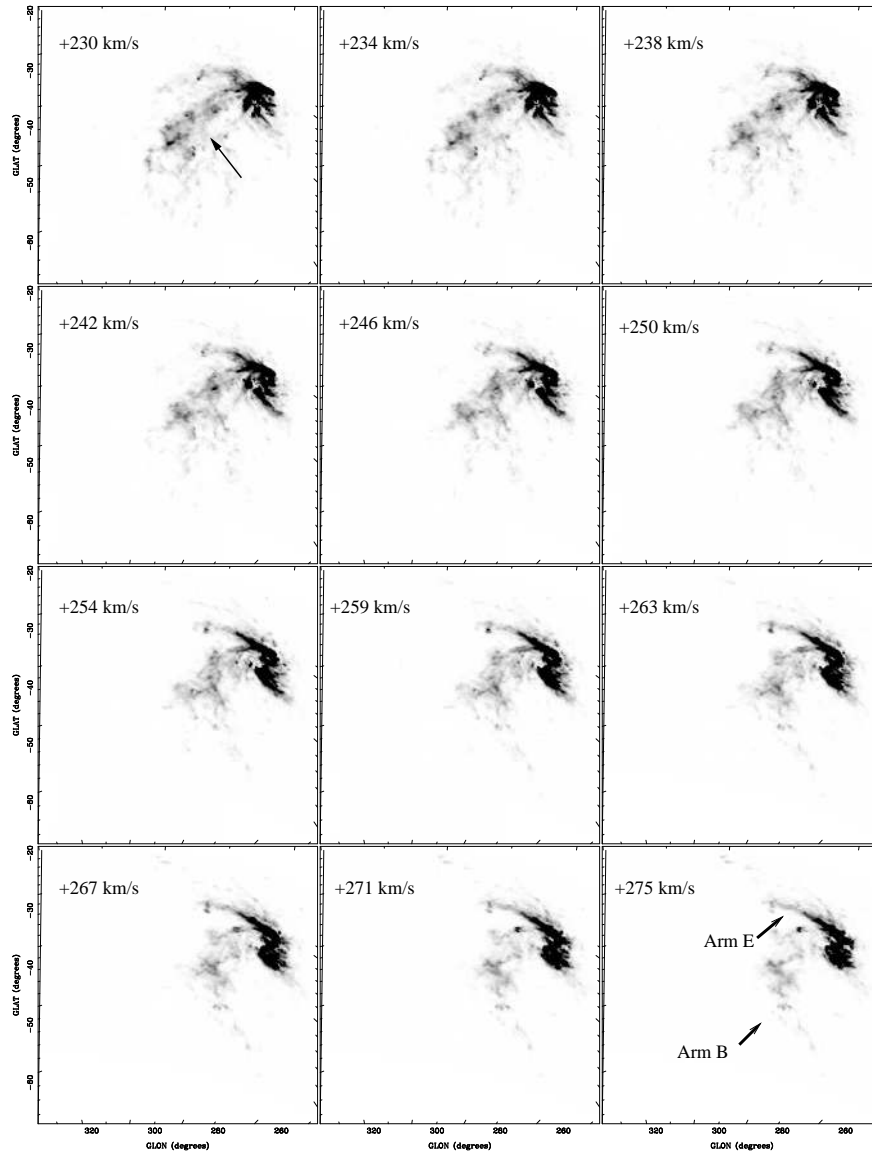
Fig. 9.— Same as Figure 8, except showing channel maps with LSR velocity from +230 km s^{-1} to +263 km s^{-1}. This velocity range is dominated by the H I gas from the LMC and Magellanic Bridge. Black arrow in +230km s^{-1} channel map indicates the location of the Magellanic Bridge where filament 1 is now mixed in. Arm E and B are labeled in the last channel map and a sinusoidal pattern is seen.
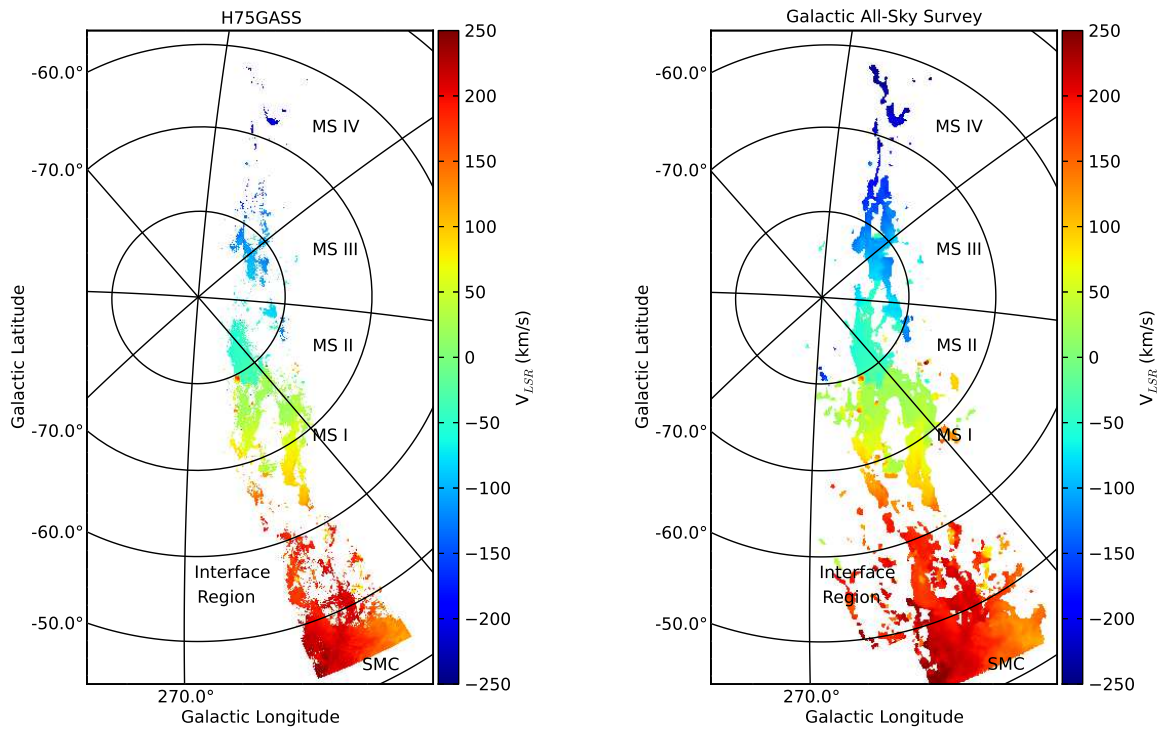
Fig. 10.— Velocity field map in the LSR frame with a velocity range from −250 to +250 km s^{-1} for H75GASS (left) and GASS (right). The Small Magellanic Cloud, the Interface Region, and MS I–IV are labeled.
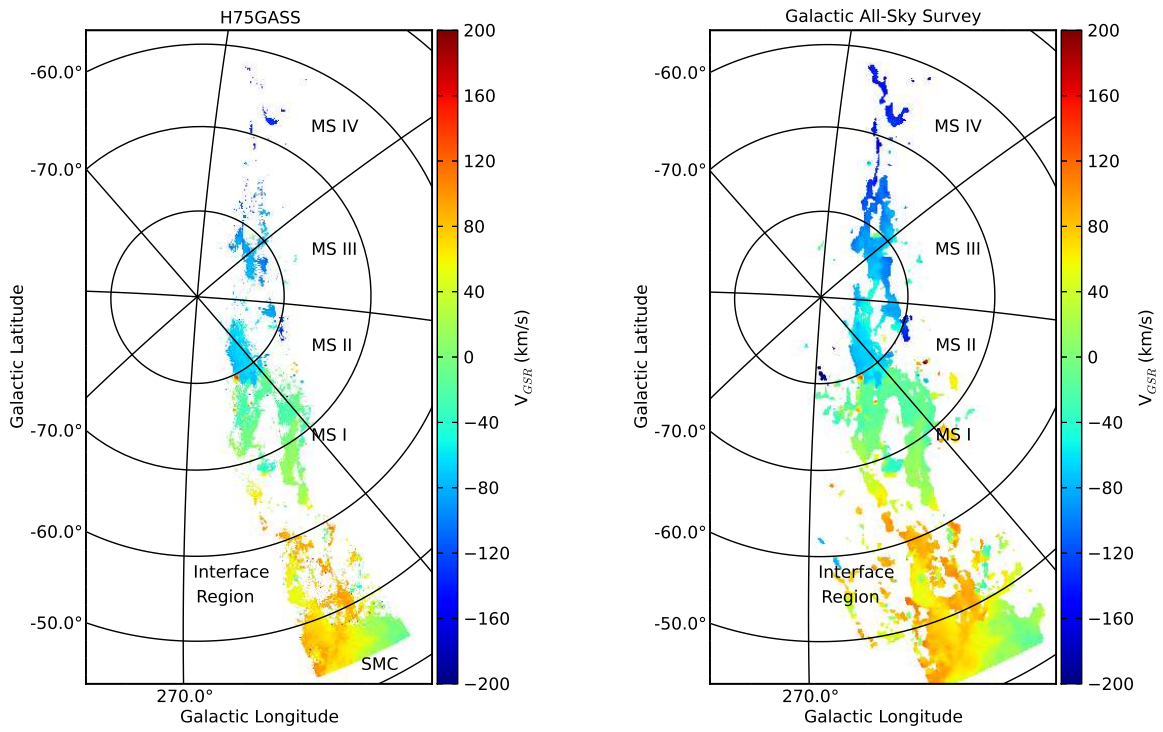
Fig. 11.— Same as Figure 10, except in GSR velocity reference frame with a velocity range from -200 to $+200$ km s^{-1}.
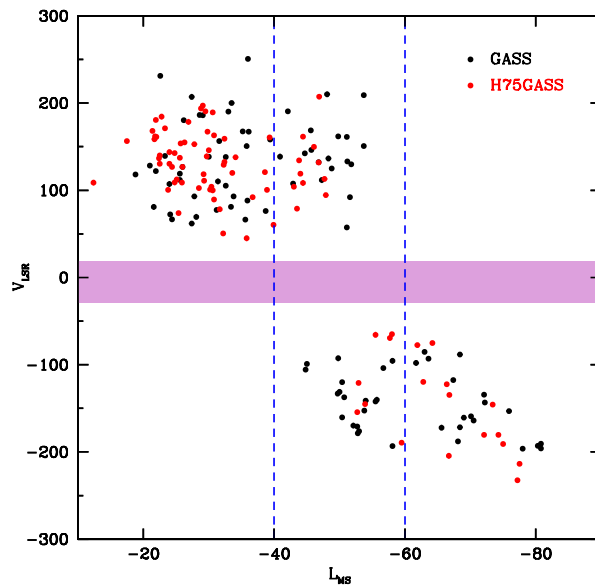
Fig. 12.— Distribution of clouds in L_{MS} vs V_{LSR}. The dotted lines mark the South Galactic Pole region. The black and red dots represent HVCs identified in GASS and H75GASS data cubes, respectively. Excluded from the plots are galaxies and HVCs that either overlap with the Galactic emission channels and/or lie at the spatial edge of the image. The shaded purple area marks the LSR velocity range from -30 km s^{-1} to $+18$ km s^{-1} that is the dominated by the Galactic gas.
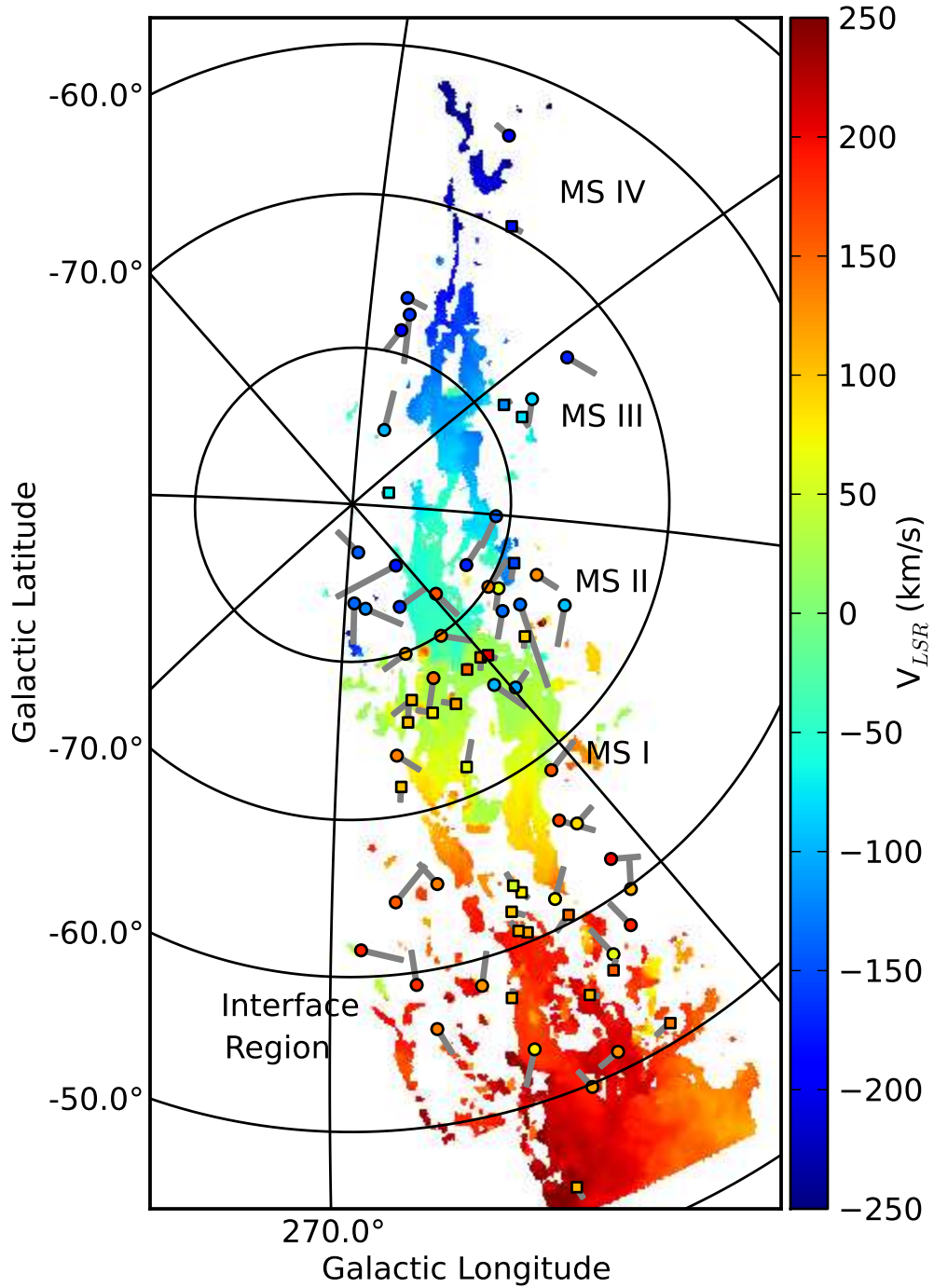
Fig. 13.— On-sky distribution of identified head-tail clouds in H75GASS (squares) and GASS (circles). The colors represent the LSR velocity of each head-tail cloud according to the color scale on the right side. The head and tail have been enlarged from their original size on the plot.
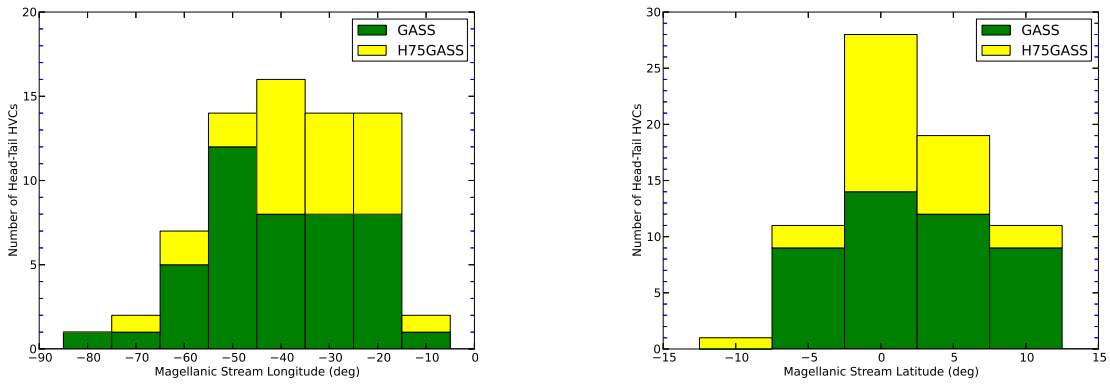
Fig. 14.— Histograms of head-tail clouds in L_{MS} and B_{MS}. The green and yellow represent head-tail clouds detected in GASS and H75GASS, respectively.
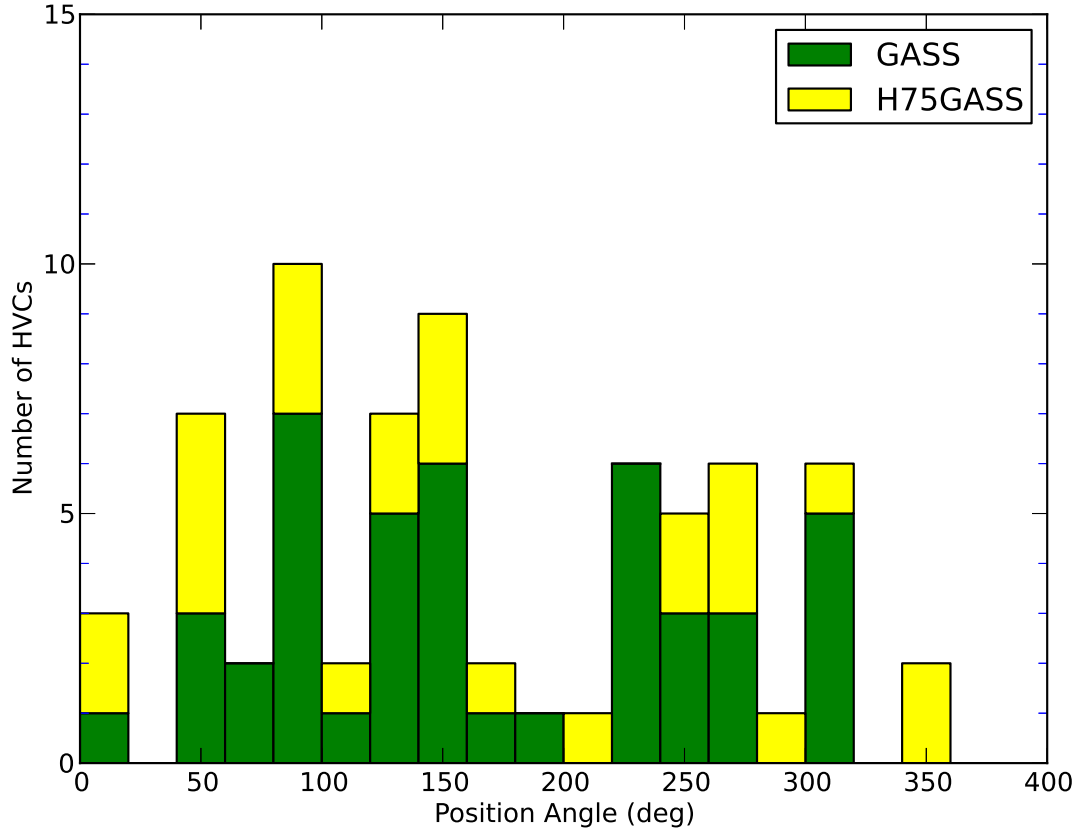
Fig. 15.— Histogram of position angles relative to the MS coordinates for all the head-tail clouds. 0° is parallel to the B_{MS} and the angle turns anti-clockwise. 90° infers the head of the cloud is pointed away from the general motion of the Magellanic System and parallel to the L_{MS}. The green and yellow represent head-tail clouds detected in GASS and H75GASS, respectively.
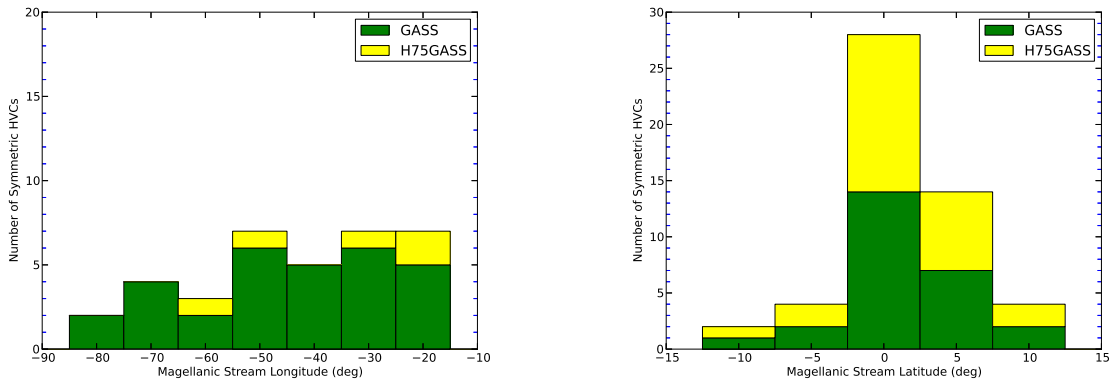
Fig. 16.— Same as Figure 14, but for symmetric clouds.
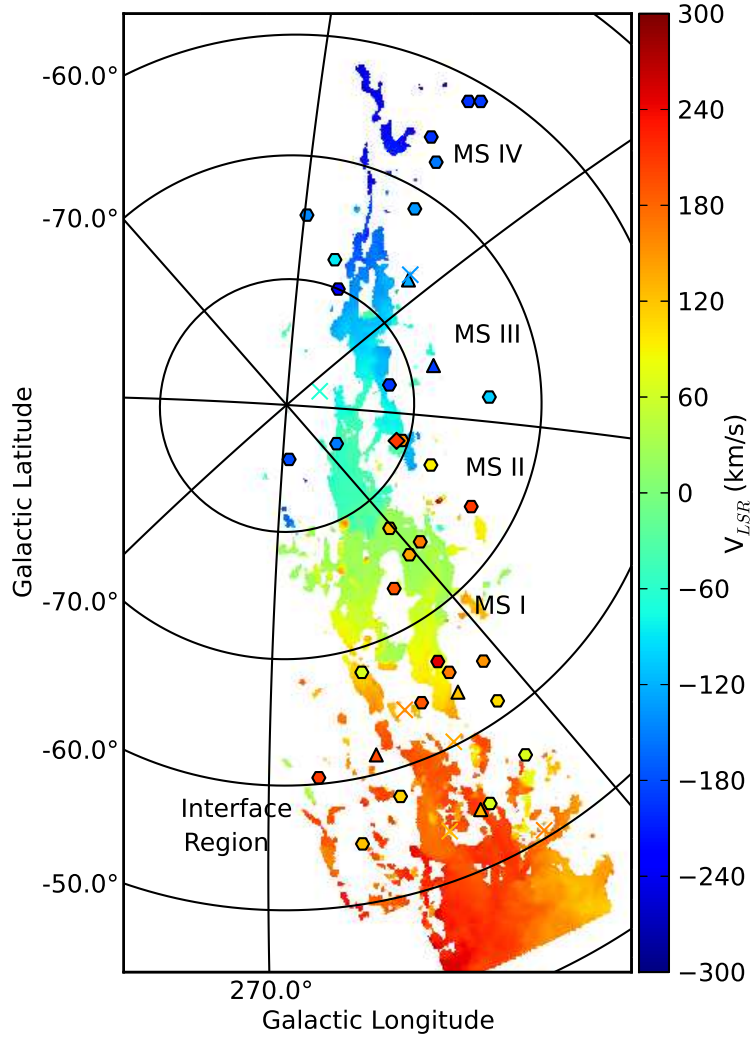
Fig. 17.— On-sky distribution of symmetric and bow-shock shaped clouds. The colors represent the LSR velocity of each cloud according to the color scale on the right side. The diamonds, and crosses represent the bow-shock-shaped clouds for the GASS and H75GASS data, respectively. The hexagons and triangles represent the symmetric clouds for the GASS and H75GASS data, respectively.

Table 1.   The velocity ranges of the original cubes and extracted subcubes.

Cube	Full V_{LSR} range (km s^{-1})	Extracted V_{LSR} range (km s^{-1})
1	$-111.45 \ldots + 382.05$	$+45.17 \ldots + 279.58$
2	$-111.21 \ldots + 382.28$	$+23.97 \ldots + 261.65$
3	$-110.55 \ldots + 382.95$	$+18.03 \ldots + 214.42$
4	$-109.61 \ldots + 383.89$	$+18.97 \ldots + 190.58$
5	$-324.38 \ldots + 330.30$	$+18.90 \ldots + 227.87$
		$-110.30 \ldots - 31.19$
6	$-323.07 \ldots + 331.60$	$-201.25 \ldots - 31.54$
7	$-320.97 \ldots + 333.70$	$-209.04 \ldots - 31.09$
8	$-318.94 \ldots + 335.75$	$-249.81 \ldots - 48.84$
9	$-317.83 \ldots + 338.88$	$-255.28 \ldots - 72.45$
10	$-315.68 \ldots + 339.02$	$-259.72 \ldots - 114.79$
11	$-314.30 \ldots + 340.40$	$-255.05 \ldots - 149.68$

Table 2.　Catalog of detected sources in the region of the Magellanic Stream.

ID	Designation $(l \pm b + V_{LSR})$	L_{MS} °	B_{MS} °	V_{LSR} km s^{-1}	V_{GSR} km s^{-1}	V_{LGSR} km s^{-1}	FWHM km s^{-1}	F_{int}[a] Jy km s^{-1}	T_{B} K	N_{HI} 10^{19} cm^{-2}	Semi-major °	Semi-minor °	PA °	Flag[b]	Classification[c]	Data[d]	Comment
(1)	(2)	(3)	(4)	(5)	(6)	(7)	(8)	(9)	(10)	(11)	(12)	(13)	(14)	(15)	(16)	(17)	(18)
24	HVC+347.9−83.8−192	−55.0	+01.7	· · ·	· · ·	· · ·	· · ·	· · ·	· · ·	· · ·	· · ·	· · ·	· · ·	SR	· · ·	G	
25	HVC+072.3−70.0−191	−75.0	−01.5	−191.0	−119.3	−079.8	21.1	12.2	1.32	2.84	0.4	0.2	17	· · ·	IC	H	
26	HVC+064.3−61.3−191	−80.8	−08.8	−190.6	−095.5	−060.4	21.0	3.5	0.23	0.36	0.2	0.2	45	· · ·	S	G	
27	HVC+019.8−78.1−189	−59.5	−04.2	−189.4	−174.0	−149.0	5.4	1.5	1.36	1.18	0.1	0.1	−67	· · ·	S	H	
28	HVC+079.6−78.5−188	−68.1	+03.7	−187.9	−144.5	−104.6	13.7	5.2	0.27	0.37	0.3	0.3	−76	· · ·	pHT	G	
29	HVC+069.2−72.8−180	−72.1	−01.1	−180.4	−119.6	−081.6	45.0	27.1	1.40	3.95	0.8	0.3	−15	· · ·	IC	H	
30	HVC+066.3−69.6−180	−74.3	−03.5	−180.3	−110.1	−073.2	22.5	9.2	1.57	3.52	0.1	0.1	78	· · ·	:HT	H	

Note. — Table 2 is published in its entirety in the electronic edition of the *Astrophysical Journal*. A portion is shown here for guidance regarding its form and content.

[a]Corrected F_{int}.

[b]SR: the detection lies at the edge of the spectral region; E: the detection is next to the spatial edge of the image.

[c]HT: head-tail cloud with velocity gradient; :HT: head-tail cloud without velocity gradient; S: symmetric cloud; B: bow-shock cloud; IC: irregular/complex cloud.

[d]H: H75GASS; G: GASS.